Broadband Antireflection Coverglass for CubeSats

by
Yaoze Liu

A thesis
presented to University of Waterloo
in the fulfillment of the
thesis requirement for the degree of
Master of Applied Science
in
Electrical and Computer Engineering

Waterloo, Ontario, Canada, 2018

AUTHOR'S DECLARATION

I hereby declare that I am the sole author of this thesis. This is a true copy of the thesis, including any required final revisions, as accepted by my examiners.

I understand that my thesis may be made electronically available to the public.

Abstract

A CubeSat is a type of miniaturized and modular satellite designed for space research or technology demonstration. By filling the unused capacity of major launch vehicles, CubeSats significantly lower the cost of entry to space.

To reduce the energy loss at the solar panel coverglass on CubeSats, we investigated the potential of the biomimetic moth-eye antireflection (MEAR) techniques which feature a gradient refractive index (GRIN). A novel fabrication process combining nanosphere lithography, reactive ion etching and dry oxidation for patterning glass with moth-eye structures was reported that allows for the production of well-defined nanopillars with tunable sidewall profiles. The thermal annealing treatment of colloidal particles was first introduced for making MEAR structures for which partial deformation of nanospheres was achieved. The broadband and omni-directional anti-reflective performance of fabricated glasses was experimentally demonstrated by using spectrophotometer and ellipsometer. A 2% and 10% decrease of reflectance throughout the measured spectral range was observed at normal incidence and high incident angles respectively.

Acknowledgements

First and foremost, I would like to thank my supervisor, Prof. Cui, for his helpful advices and suggestions. I have benefited a lot from his insight and knowledge during the two years. Without his guidance this thesis would not have been possible.

I would also like to express my gratitude to Prof. Regina Lee at York University for her support of this research, and Dr. Hugh Podmore for his innovative ideas and instructions. My appreciation extends to the Quantum NanoFab, WATLab, Giga-to-Nanoelectronics (G2N) and Centre for Advanced Photovoltaic and Display Systems (CAPDS) at university of Waterloo, for their technical support and allowing me access to the nanofabrication and characterization facilities.

To my group mates especially Mohammad Soltani, Hirotaka Yamada, Ferhat Aydinoglu, Ripon Dey, and Ruifengyang, thank you all for the beneficial discussions and helping hands.

Dedication

To my family, for their devotion and endless support.

Table of Contents

List of Figures

List of Tables

Chapter 1 Introduction

1.1 Motivation

Although the exploration of space traces back to ancient times when it solely comprises the observation of objects with naked eyes, it was the development of modern technology that made physical exploration possible. In the year 1957, the world's first artificial earth satellite "Sputnik-1" was launched by the Soviet Union, triggering the passionate Space Race Era during which hundreds of satellites were employed for the proof of dominance in spaceflight capability. According to the United Nations Office for Outer Space Affairs (UNOOSA), there are 4817 satellites[1] currently orbiting the planet, mostly serving the purposes of weather diagnostics, communication, navigation, earth and astronomical observation.

Over the years, space exploration has become near exclusively government supported projects. There are numerous reasons for the long-standing dominance of government agencies on earth's orbit, but principally are the high financial, technical and regulatory barriers. However, this situation began to change as the rapid development of small satellites significantly lowers the total cost of deployment. Carried by the excess capacity of larger launch vehicles, miniaturized satellites such as smallsats (mass less than 500 kg), microsats (mass less than 100 kg) and nanosats (mass less than 10 kg) are increasingly welcomed in ride-sharing programs. The advantages of much less financial costs on launch vehicle preparation, costs associated with design and construction, the capability of achieving certain purposes (such as gathering scientific data and technology demonstration) encourage private companies, universities as well as other developers to actively participate in the development of miniaturized satellites.

Among all those small satellites above, CubeSats, which falls into the category of nanosats, saw a significant growth with continued advances in the miniaturization and capability of electronic technology. The CubeSat is a type of small modular satellites that usually consists of single or multiple 10 x 10 x 10 cm^3 standard cubic units, with one unit close to 1 kg and not to exceed 1.33 kg[2]. Figure 1.1 shows a typical communication CubeSat built by students of the University of Tsukuba. "1U" CubeSat refers to a CubeSat that comprises of only one cubic unit, with multiple units as 2U, 3U and so on. Instead of using custom-built components for each mission, the modular nature of CubeSats allows for choosing commercial off-the-shelf (COTS) components for their structure and electronics, also further lowers the cost of entry. These features make CubeSats an ideal platform for both commercial and academic projects; typical applications are communications, earth observation, technology demonstration and scientific research.

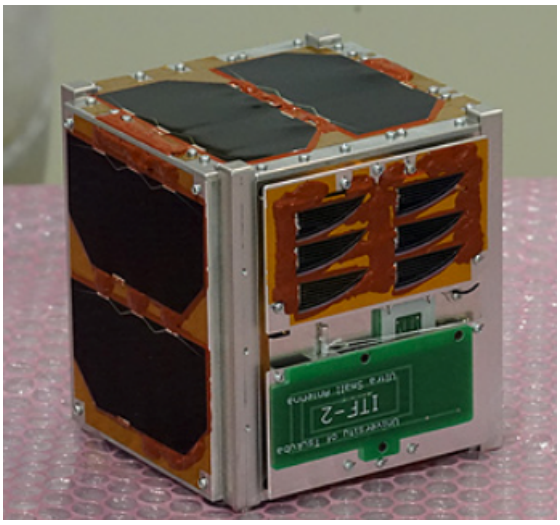

Figure 1.1 Picture of ITF-2 (Imagine The Future 2) built by the University of Tsukuba[3].

It has been reported that just nine years after the first launch in 2003, more than three hundred CubeSat-class satellites have flown, fielded by nearly 80 organizations from 24 countries on 29 rockets[4]. Growth at double digit rates is predicted to continue in the future driven by the

commercial and academic operators. Figure 1.2 presents a chart of nano/microsatellite launch history and forecast[5] released by Spaceworks Enterprises, Atlanta. Being largely favored by rideshare missions, nanosatellite (1-10 kg) consisting of 1U and 3U CubeSats account for the majority of both historical and planned launches.

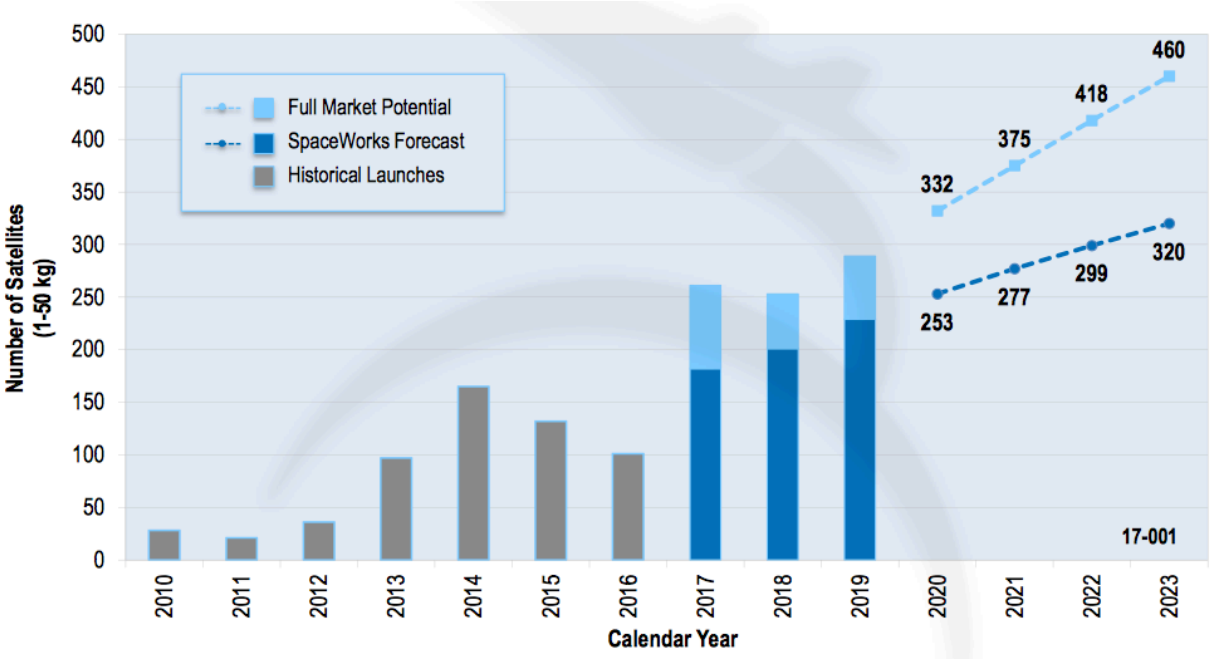

Figure 1.2 Nano/Microsatellite launch history and forecast (1-50kg) by Spaceworks Enterprises[5].

For a nanosatellite made up of several CubeSat units, regardless of its primary scientific or technical objective, the lack of sufficient power generation and storage abilities has always been one of the major challenges in the design and construction process. Unlike conventional satellites for which deployable sun-tracking solar arrays is the common option for electrical power supply, 84% of nanosatellites[6] are using body-mounted solar panels instead due to its small volume and weight. An example would be the ITF-2 shown in Fig. 1.1. It is obvious that small solar cell pieces are tightly mounted on the left, top, and front surface of the CubeSat. In this case the surface area for power generation is significantly limited. In addition, the absence of sun-tracking arrays further

affects the power generation ability of CubeSats since body-mounted panel will often experience high angle of sunlight incidence. On the other hand, attitude and orbit determination and control system (ACS), communication module, and scientific devices on board all require high levels of power draw for the accomplishment of the mission. In fact, power sub-system failures account for 17% of mission failures between year 2000-2012[4]. It is one possible option to increase the power storage for nanosats since power generation is limited by the factors above. However, this is not a desirable solution because larger batteries would not only occupy more space, the increased weight also impose restrictions on the launch vehicle choices. Given that the nanosat missions tend to have short operational and orbit lifetimes, the outcome will very much be determined by the ability to generate power rather than to store it.

Another option for CubeSat developers is to improve the solar cell efficiency at high angle of incidence. However, space industries and photovoltaics are two different fields separating from each other, and in the part the focus does overlap is the traditional satellites. For them the consequence of power deficit at high incidence angle to the sun is of little concern when sun-tracking panel can be equipped. As to CubeSat developers, they tend to purchase COTS solar cells directly from suppliers and possess neither the capability nor willingness of addressing the issue of power generation at the solar-cell level.

1.2 Organization of the Thesis

It has been demonstrated that subwavelength structure (SWS) fabricated on silicon (Si), gallium arsenide (GaAs), and silicon nitride (SiN_x) successfully improve the power conversion efficiency of solar cells[7-11]. The SWS significantly suppresses the reflective loss of light over a wide spectral range, which is beneficial for solar cell because solar energy is mostly distributed

throughout the UV-VIS-NIR wavelengths. Recently, moth-eye-like antireflection (MEAR) --a subset of the SWS--has been extensively explored for its superior anti-reflective performance. This gives new directions to reduce the reflection for various applications. Compared with conventional single layer antireflection coatings (ARCs), moth-eye structure offers effective broadband antireflection properties over a wide range of incidence angle[12]. These advantages of moth-eye antireflection are particularly attractive to CubeSat developers because the body-mounted cells on CubeSats are expected to experience very high angles of incidence to sunlight during operation. To protect cells from radiation damage in space, CubeSat developers commonly deploy a coverglass on top of the COTS cells[13]. By applying MEAR techniques to the coverglass, it is possible to increase the external quantum efficiency (due to the reduced reflection) of the solar cells and thus improve the power generation. Moreover, the fabrication of moth-eye structure on coverglass would place no additional demand on the mass or volume of the CubeSat, and raise no concern of electrical characteristic degradation of cells[14] with no fabrication procedure conducted at solar cell level. Past work using MEAR techniques for CubeSats was unclear, but related work in which moth-eye structures on transparent substrates were proven have broadband antireflection performance at normal incidence. Although the fabrication routes and materials were different, 1.5% and 2% improvement of broadband antireflective performance by nanopillars of various periods were achieved in [15] and [16], with the maximums of 10% improvement at 600 nm in [17] and 5% improvement from 480 nm to 530 nm in [18].

The majority of fabrication processes developed for subwavelength antireflection (SWAR) and moth-eye antireflection (MEAR) structures so far are unsuitable applied to the transparent glass because of its high etching resistance. For polymeric antireflective structures, despite the ease of patterning is an advantage compared to the glass substrate, the fabricated structures are of

poor robustness and low stability for space applications where UV irradiation could result in slow changes in the properties of polymers. It is therefore a meaningful task for the development of CubeSats with the coverglass treated with MEAR technique to reduce the energy loss to improve the overall power generation. In considering to the achievement reported in [15-18], it is reasonable to set our goal of a 5% decrease in a wider spectral range, more importantly, the enhanced antireflective performance should also be achieved when the incident angle increases.

This thesis is separated into six chapters. Chapter 1 gives brief introduction about the emerging field of CubeSats, and discuss the reasons and prospect of developing MEAR coverglass for body mounted solar cells on the CubeSats. Chapter 2 describes the background and compares the conventional thin film antireflection techniques and the moth-eye technique. Chapter 3 introduces several nanofabrication techniques that involves in the fabrication of moth-eye surfaces. Chapter 4 details the proposed novel fabrication process, with investigation on the process conditions. Chapter 5 presents and illustrates the optical reflectance measurement results. Chapter 6 summarizes the thesis.

Chapter 2 Antireflection Methods

2.1 Thin Film Anti-Reflective Coatings

Anti-reflective (AR) film is a well-developed and simple technique to enhance the light transmission first proposed by Lord Rayleigh[19]. Thin AR coatings are commonly used in applications where low loss or reflection is desired at the optical surface, and the examples include camera lens, solar cells, corrective lenses and other optical instruments. A typical AR film consists of a single layer of transparent material sandwiched by two different media. With the value of refractive index (RI) n_l somewhere between that of the two surrounding media (n_0, n_s), the AR film acts as an intermediate layer and can be thought of as to the technique of impedance matching in electrical systems. Optimal antireflection will occur when the refractive index is given by the geometric mean of the surrounding indices:

$$n_l = \sqrt{n_0 n_s} \tag{2.1}$$

The anti-reflective performance is further enhanced by taking advantage of destructive interference effect. Shown schematically in Fig. 2.1[20], incoming light with a wavelength of λ arriving from air towards the coating (refractive index n_l larger than n_0) will be partially reflected at the front surface, with a π phase change of the reflected ray R1; the rest continues to transmit before reaching the interface between the coating film and substrate (refractive index n_s larger than n_l), partial reflection occurs again, producing another reflected ray R2 with a phase change of π. Therefore, there is no component of phase difference due to reflection, and at the time R2 travelled back to the front surface of coating, the total phase difference $\Delta\phi$ between R2 and R1 is solely determined by the path difference, which is a round trip through the film. For the case that

the incoming light is at normal incident angle and the thickness of the AR film is precisely engineered by

$$t = \frac{\lambda_l}{4} = \lambda_0/4n_l \tag{2.2}$$

then at the front surface where the two reflected beams meet, the phase difference $\Delta\phi = \pi$ since R2 travelled $\lambda_l/2$ further and reflected light R1 and R2 are out of phase. So, for this wavelength λ_0, destructive interference occurs and only little power is reflected from the coated film. This technique is also named quarter-wavelength coating due to the geometry of the AR film.

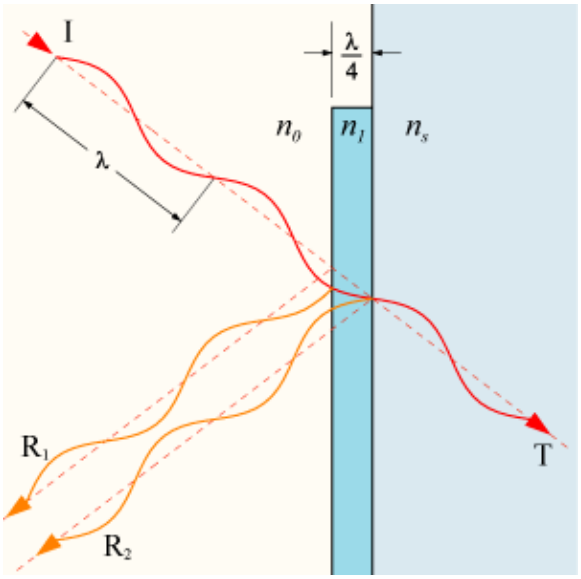

Figure 2.1 A schematic of the reflection/transmission process of light entering the quarter-wavelength AR film [20]

For quarter-wavelength coating, the anti-reflective performance strongly depends on the wavelength of incident light. With the lowest reflection occurs at only one distinct wavelength of light, the performance gets worse when the wavelength of incoming light deviates from λ_0. One can overcome this drawback by introducing a stack of AR coating layers. Ideally the reflection from all interfaces interferes destructively and reflection at different wavelength will be further

reduced. However, it is difficult to precisely control the thickness of each layer, and more importantly the thermal mismatch and poor adhesion between layers are the major challenge in outdoor applications let alone in space environment.

Regardless of the number of coated layers, the anti-reflective capabilities of interference film coatings degrade when the light is not at normal incidence (incoming light ray not perpendicular to the substrate surface). This is because that the reflected ray of tilted light exits the film with a spatial offset from the spot it entered, and interferes with reflection that travels further; as a result, the phase gained in the film relative to the phase of light reflected at front surface decreases with the angle of incidence. Last but not least, according to equation 2.1, materials with low refractive index are desired for the perfect antireflection. However, there is only a few materials in nature that has a low-index and also features good physical properties for a coating process.

2.2 Moth-eye Antireflection Technique

An alternative to the conventional coating methods is to pattern the surface with periodically nano-structured array, which is the subwavelength antireflection (SWAR), so that the periodicity is smaller than the wavelength of incident light. As a biomimetic technique, the idea of this originates from the observation on the corneas of some moths in the year 1973. Electron microscope, as shown in Fig. 2.2[21], reveals that the outer surface of their corneas is covered by a regular array of conical protuberance (typically with a height and spacing about 200 nm) , suppressing diffraction by offering a graded refractive index between the air and the corneas and thereby reducing the reflection across a relatively large spectral range[22]. Although the reflection increases at long wavelengths----when interface thickness is small compared to the wavelength, and short wavelengths--when structures are no longer subwavelength and are diffractive, such sub-

wavelength structure (SWS) allows the nocturnal moth to see well in the dark, without the risk of causing reflection that will give away its location to the predators. The realization of low reflection by nature using moth-eye arrays have inspired many attempts to mimic such pattern. Ever since then there have been significant achievements in research on methods for fabricating the moth-eye antireflection structures, such as electron beam lithography, interference lithography and nano-imprint lithography.

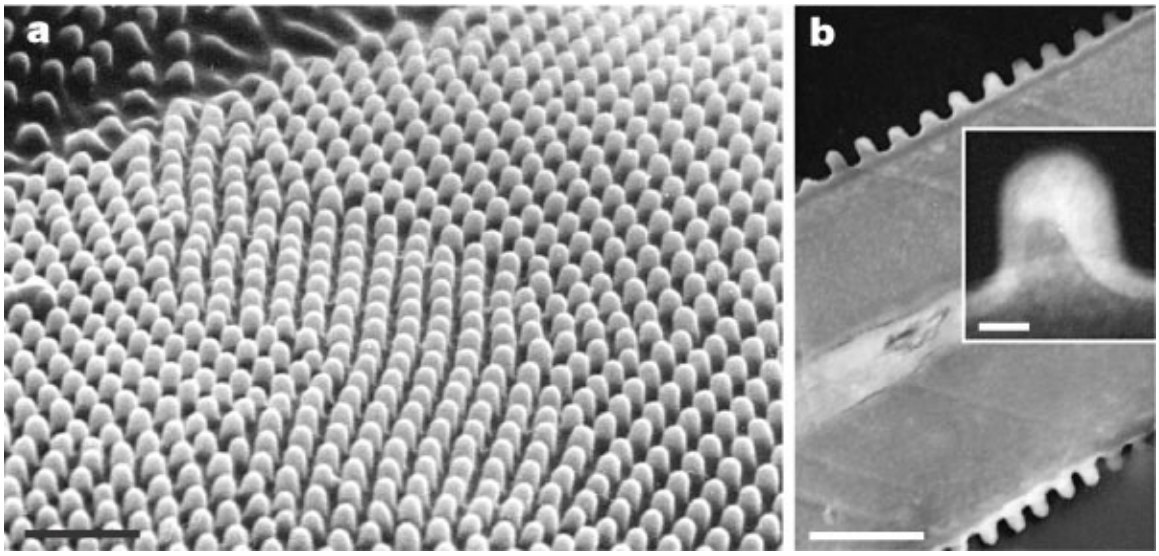

Figure 2.2 Scanning electron microscopy (SEM) images of the anti-reflective nipple arrays on (a) corneal surfaces of a lepidopteran eye; (b) the transparent wings of certain hawkmoths. The inset image shows the magnified profile of a single nipple. Scale bars, a, 1 μm; b, 1 μm; inset, 100 nm [21].

To understand the principle of MEAR, it is helpful to start with a simple case of 1D grating which also consists of periodic structure. Fig 2.3 shows the sketch of a 1D grating with a period, d, illuminated by a parallel beam of monochromatic light with wavelength λ at incident angle θ_i. Light is diffracted into different orders each at a diffraction angle θ_m given by

$$\theta_m = \arcsin\left(\frac{m\lambda}{d} - \sin\theta_i\right) \tag{2.3}$$

where m is an integer of the diffraction order. For simplicity, we first consider the case that light comes at normal incidence, which means $\theta_i = 0$, then the sinusoidal term inside bracket will disappear. Further we assume that the grating period is sufficiently small ($d < \lambda$), and it is obvious there is no real solution for θ_m where $m > 0$. This means that at normal incidence, the diffraction orders above 0-th are strongly suppressed and the reflection will be purely specular. Similarly, when $d < \frac{\lambda}{n}$, transmission will be specular since orders diffracted are suppressed inside the material[22]. However, for oblique incidence higher diffraction orders can emerge. Considering that the first order to disappear (diffracted at an angle greater than 90°), a more stringent condition on the grating period d can be given to ensure no diffraction over all angles of incidence when it satisfies that $d < {}^{\lambda}/_{2n}$[23], where n is the refractive index of the grating material. If this condition is fulfilled light is unable to resolve the grating structure; instead it only perceives a region that the refractive index is gradually changing at different depth which is guided by the Effective Medium Theory (EMT) [12, 24-28].

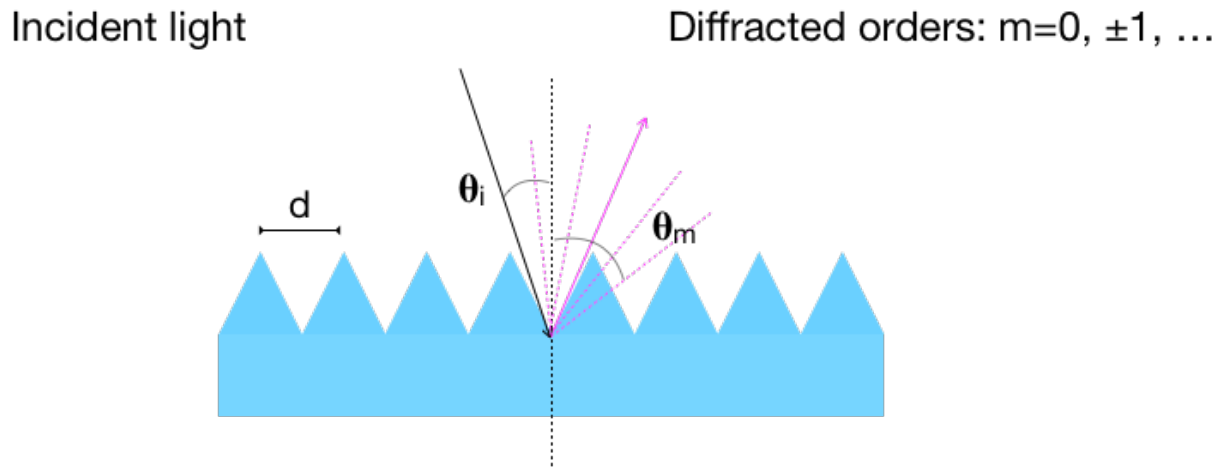

Figure 2.3 1D diffraction grating illuminated by monochromatic light.

Theories applicable for surface with grating-like geometry can be categorized into four groups according to the periodicity (Λ) with respect to the wavelength (λ) [26], as shown in Fig. 2.4, moth-eye shaped structures generally belong to the region governed by the effective medium theory.

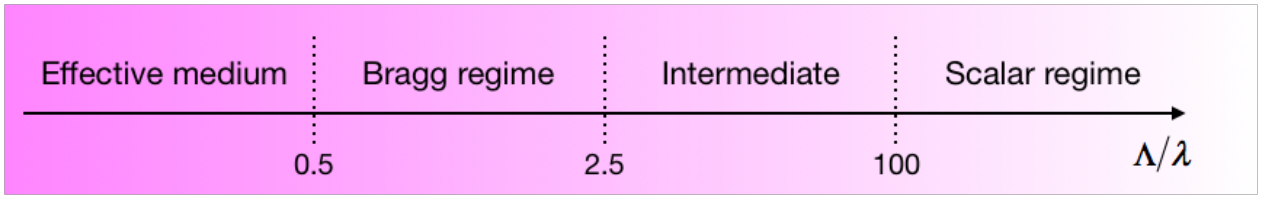

Figure 2.4 Theories applicable for structures with different Λ/λ ratio [26].

The subwavelength regime or the long wavelength limit indicates that if the period of structure is smaller than wavelength, electromagnetic waves will propagate in a heterogeneous mixture as in an homogeneous medium with an anisotropic distribution of dielectric permittivity[29]. That is, the effective refractive index (n_{eff}) of the moth-eye structure is determined by the optical properties of the air/structure mixtures[30]. It is therefore available to have the effective refractive index n_{eff} as a function of fill factor f following the two-dimensional Bruggeman formula[31], shown in eq 2.4:

$$n_{eff} = \left[f{n_s}^{2/3} + (1-f){n_0}^{2/3}\right]^{3/2} \tag{2.4}$$

Where n_s and n_0 are the refractive indices of nano-structure and air, respectively, fill factor f represents the fraction of volume taken by the structure in a horizontal slice. To qualitatively understand how n_{eff} changes with the other two media, eq 2.4 can be well approximated by a simple weighting formula[27]:

$$n_{eff} = fn_s + (1-f)n_0 \tag{2.5}$$

In the case of cone or paraboloid pillar structures shown in Fig 2.2, f gradually increases through the structure from the top where air accounts for the most area to the bottom where area is mostly taken by the structure. As a result, the value of n_{eff} also exhibits a continuous subtle increment vertically from pillar tops to pillar bottom. Fig 2.5 illustrates two different types of sub-wavelength structure and their corresponding refractive indices in the long wavelength limit ($\Lambda \ll \lambda$) [32].

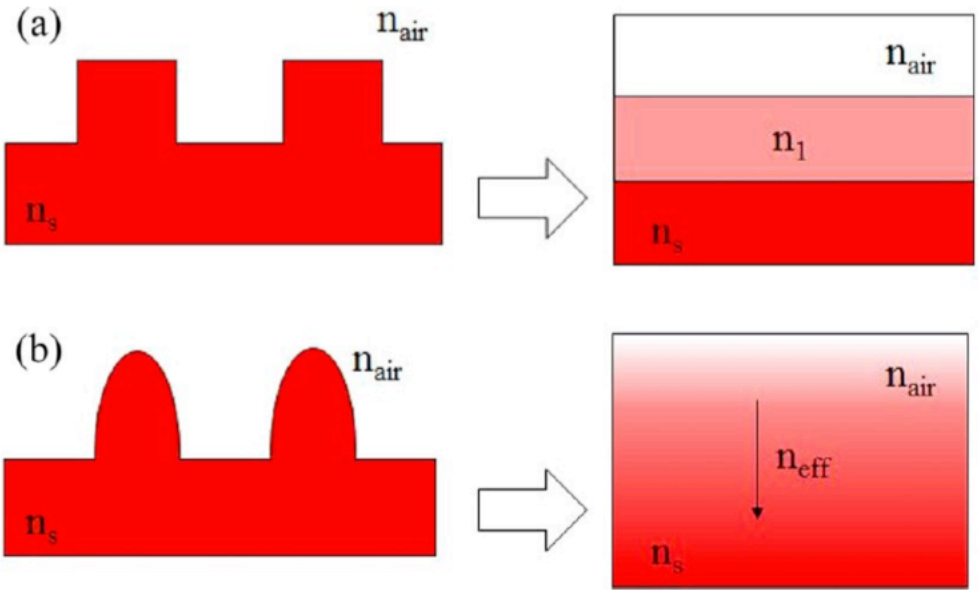

Figure 2.5 Schematics of the sub-wavelength structures and their analogous refractive index profiles, as experienced by incident light: (a) ridged profile; (b) parabola-shaped profile [32].

For Fig. 2.5(a), electromagnetic waves interact with surface textured by ridged nano-structures as if it's a conventional coating layer, with a fixed value of refractive index determined by the ratio between the channels and structures; for Fig. 2.5(b), moth-eye like structures behave as an infinite stack of ultra-thin layers, with effective indices of each layer gradually increase from n_{air} to n_s, and thus forming a gradient refractive index (GRIN) region. The GRIN region

effectively smooths the transition across interfaces of different media and eliminates the mismatch of refractive index. Hence, incident light propagating in the GRIN region does not experience a sudden change in the refractive index, and reflection at any particular depth will be substantially reduced over a broad range of angles as well as wavelengths. The increasement of fill factor "f" is determined by the taper angle. With a moderate angle, the fill factor increases smoothly through the top to bottom and so does the effective refractive index, light reflected at each slice will have a phase determined by the distance traveled through the structure. The more phases, the more possibilities of undergoing destructive interference and yielding low reflection for broadband and wide-angle light[12, 16, 26].

The antireflection effect of moth eye technique should not be confused with that of surface roughening. In fact, rough surface merely achieves the redistribution of reflection because of diffuse scattering and degrades the transmitted wavefront of light[22]. In terms of moth-eye effect, diffuse scattering is not increased, the transmitted wavefront is not degraded either, and reduction in reflection directly leads to the increase in transmission.

Chapter 3 Special Techniques for the Fabrication of Moth-Eye Structures

In the previous chapter the realization of broadband and quasi-omnidirectional antireflection by moth-eye structures was discussed. The MEAR nanopillar arrays behave like a homogeneous film featuring a gradient refractive index (GRIN) since incident light cannot resolve individual structure in the long wavelength limit. To provide a smooth transition between interface of the surrounding media, an ideal moth-eye textured surface should be completely and uniformly covered by the ultra-fine moth-eye structures that has a period much less than the range of wavelengths. For the case of CubeSats applications, it also brings up the requirements that structures along with the glass substrate should be resilient to radiation damage in the space environment and have a great tolerance to the drastic change of temperature during operation. In this chapter, various techniques involved in the fabrication of such MEAR surface are illustrated.

3.1 Overview of Nano-Fabrication

The space between individual structure or the pitch of the structure is the fundamental geometric constraint for MEAR antireflection. In order to form GRIN region, it is necessary that the pitch satisfies $\Lambda < {}^{\lambda}/_{2n}$[18]. Therefore, to realize the potential of MEAR, fabrication has to be performed at the nanometer scale.

Nanofabrication techniques are commonly classified into two principle approaches. The first one is “top-down” approach, which involves a sequence of additive and subtractive step with various lateral patterning throughout the process. The pace of miniaturizing continues towards the

final structures. In contrast, for "bottom-up" approach, direct guided- or self- assembly occurs at very small scale to create larger scale structures with engineered properties. Figure 3.1 shows two typical cases of top-down and bottom-up processes[33].

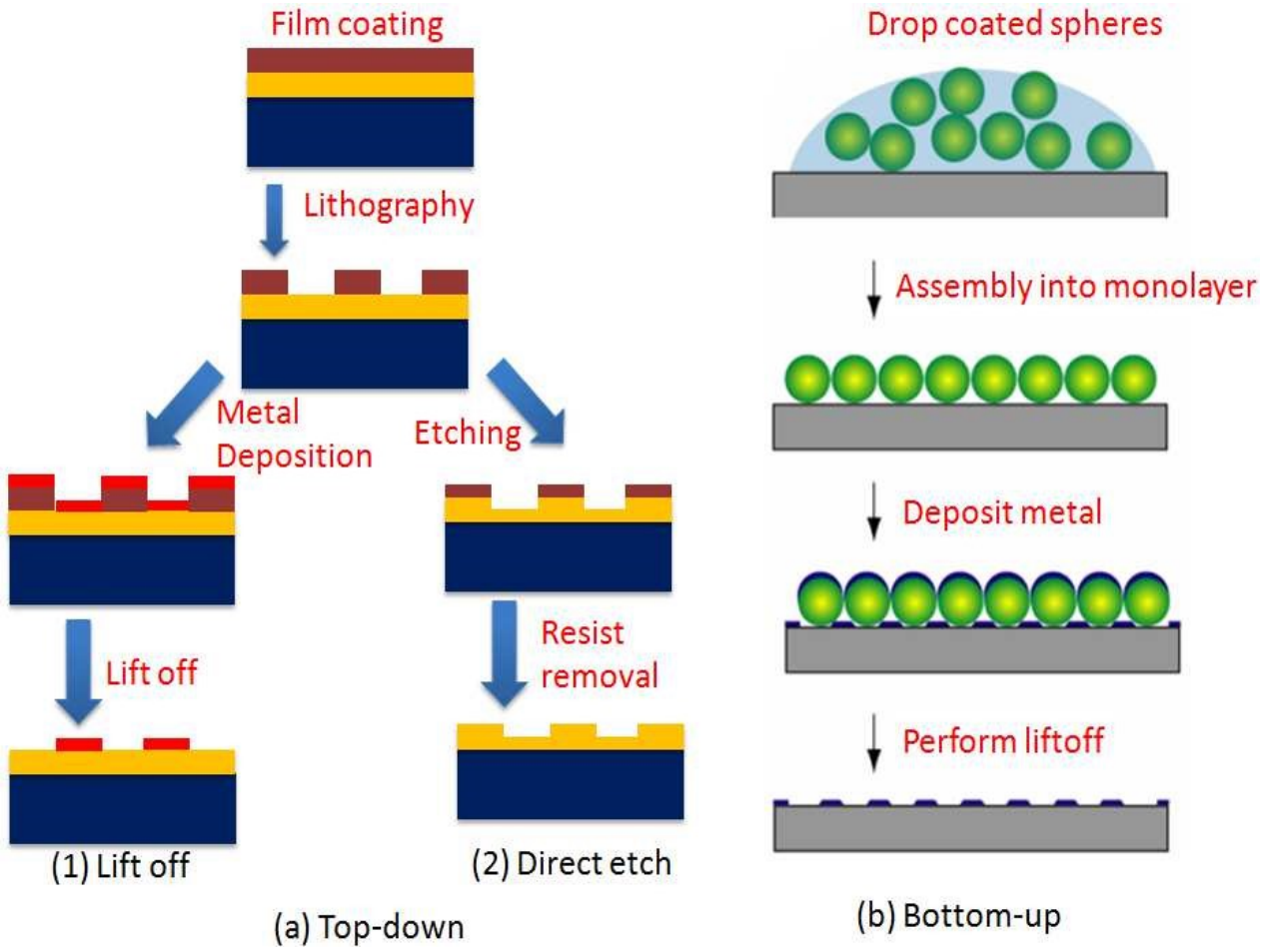

Figure 3.1 Schematics of the (a) top-down and (b) bottom-up approach. In the top-down approach, lithography is performed after the coating of resist, pattern can then be transferred either by (1) a deposition and lift-off route, or (2) direct removal of materials, namely, etching. In the bottom-up approach, initial pattern, monolayer of nanospheres, is achieved by self-assembly; secondary pattern is then made by metal deposition and a lift-off step on the substrate [33].

In reality, these two approaches are often used altogether in a nanofabrication process because of pros and cons associated with them. Thanks to the development of lithography techniques,

various designs of structures can be made from top-down process. Another advantage is the great consistency of structure quality; top-down process is therefore favored for large scale production. However, high-precision top-down fabrication typically relies on state-of-the-art facilities which are quite expensive. In comparison, fine structures with certain arrangement could be made by bottom-up process at a much lower cost without lithographic steps. However, the disadvantages of bottom-up approach including lack of flexibility in terms of pattern design and low throughput limit its industrial applicability. Overall, one should wisely choose the fabrication that best fits to avoid unnecessary cost on time and funds.

For the production of MEAR surface for CubeSats application, the top-down process is preferred due to its inherently great robustness and its favorable chemistry against atomic oxygen bombardment in space[13]. Both additive and subtractive steps play important roles in the fabrication process and will be discussed in the following content.

3.2 Thin Film Deposition

In the field of nanofabrication, addictive steps are normally done by a variety of thin film deposition methods, and examples are physical vapor deposition (PVD), chemical vapor deposition (CVD) and spin coating.

3.2.1 Evaporation

Vacuum thermal evaporation is one of the physical vapor deposition methods, and is widely used for the deposition of metal or dielectric materials in both industries and laboratories. Fig. 3.2 shows the picture of an R&D evaporation system, Nanochrome^{TM}, provided by the Intlvac Thin Film Corporation[34]. The process of deposition by evaporation is not complicated: in the medium to high vacuum range of 10^{-5} to 10^{-9} torr, high purity source material is first heated up above a

certain temperature, atoms of the vaporized material then travel freely inside the chamber before condensed on the substrate.

Figure 3.2 Picture of the Nanochrome™ evaporation system [34].

As shown in Fig. 3.3, there are two types of evaporation in terms of the methods of heating the material. The first is resistance heating technique, where the target material is heated by the flow of direct or alternating electrical current through a filament. Some other means of heating is also used, such as boron nitride crucible surrounded by RF coil. The resistance heating has a simple configuration and is good for depositing metals or some organic compounds with low melting temperature. One major drawback is that the filament or crucible is heated together with the materials inside during evaporation, resulting in high impurity in the film.

The other is the electron beam technique, where heat is generated by high energy electron beam bombardment on the target. Electrons emitted from an electron gun are accelerated by high electric potential. With the applied magnetic field, electron beam can realize localized heating on the target material. This allows for the precise control of evaporation rate, and a lower risk of contamination since the crucible is not heated.

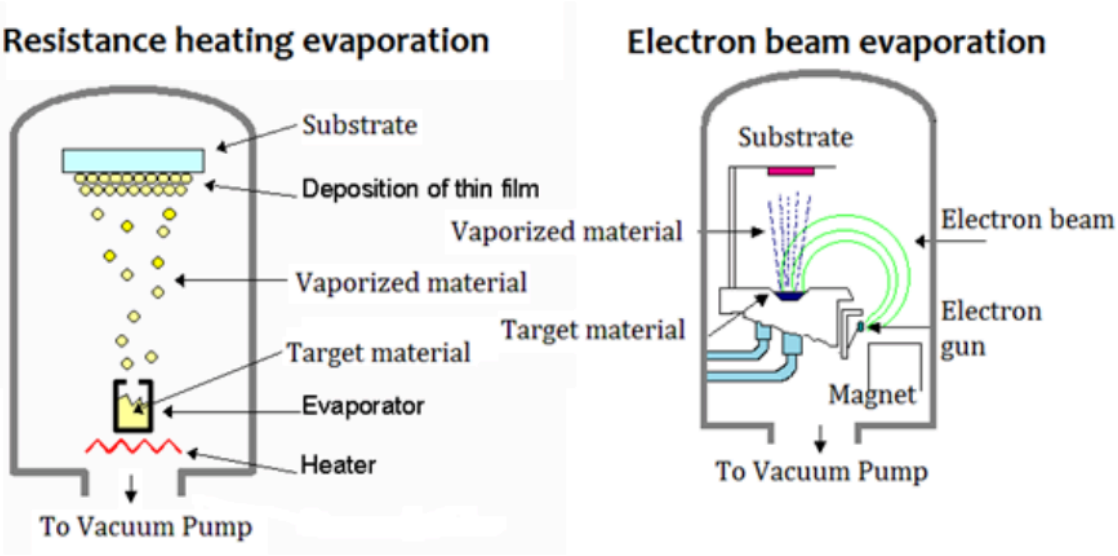

Figure 3.3 Schematic of resistance heating (left) and electron-beam heating evaporation (right) [34].

As the oldest technique, evaporation is still an effective thin film deposition technique. Although modern techniques such as sputtering saw a growing popularity in the industries, advantages of evaporation like low cost, simplicity and versatility are beneficial for research and development purposes.

3.2.2 Sputtering

Sputtering deposition is another PVD method of thin film deposition, where gaseous plasma is involved. In a direct current (DC) sputtering process, target material is bombarded by the ionized gas molecules such that atoms from the material are emitted/sputtered off the target into the plasma,

vaporized atoms are then condensed on the substrate to be coated. Fig. 3.4 illustrates the different regions and the corresponding names for a DC glow discharge[35]. Reducing the gap between electrodes will result in fewer regions; in fact, the positive column will totally disappear when the gap is small enough and the discharge is primarily a negative glow region sandwiched by two dark regions.

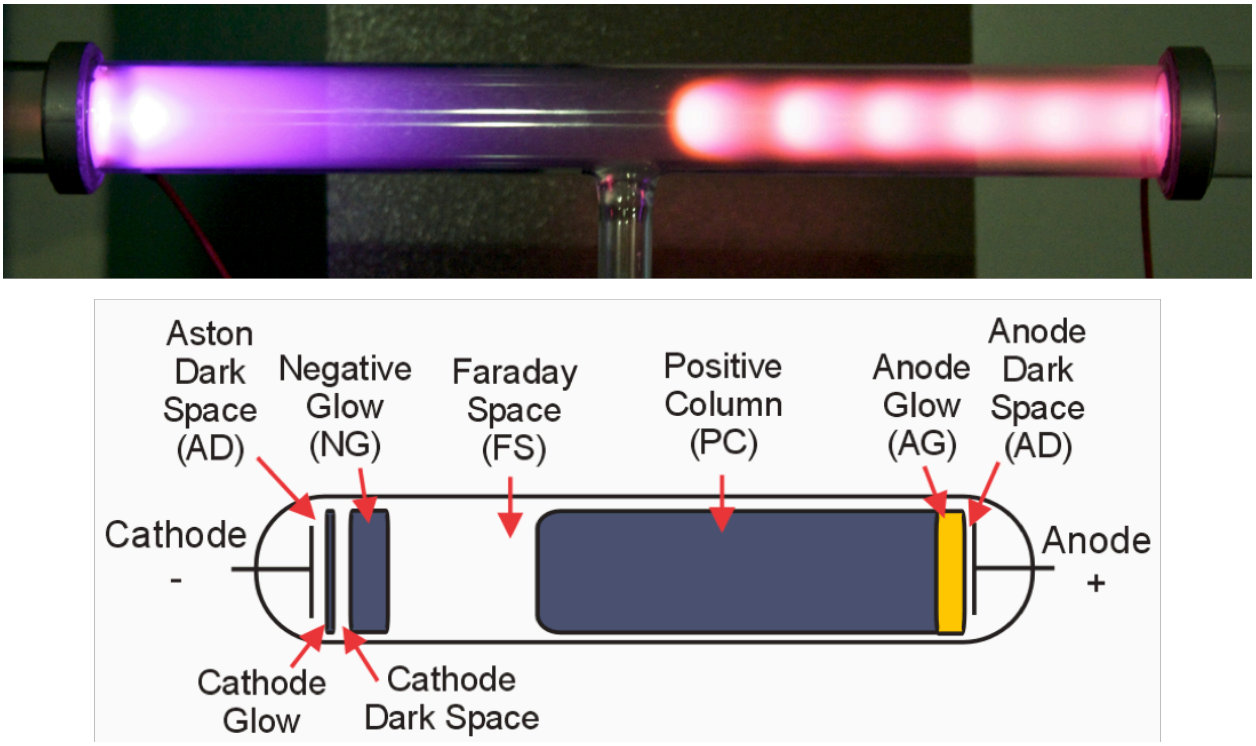

Figure 3.4 Illustrations of the main regions present in a glow discharge, where regions annotated as "glow" emit bright light whereas "dark space" doesn't [35].

DC glow discharge is the simplest type of glow discharge. With adequate DC voltage applied to the two electrodes at the two ends of a tube, glow discharge will occur when the tube is kept at a low pressure such that charged particles can gain sufficient energy before colliding with the other particles. Ionized gas molecules with positive charge are accelerated towards the cathode by the electric potential. Ions with enough kinetic energy striking the cathode will cause the sputtering

process, in which atoms at the surface of cathode are ejected into vacuum environment with sufficient energy to reach and get deposited on the anode. In order to facilitate the numbers of high energy collisions, gas inside the chamber (or tube) is usually chosen to have a high molecular weight, such as argon.

Strong magnets are often used at the cathode to trap electrons in the plasma close to the target, which is known as magnetron sputtering. Shown in Fig. 3.5[36], with the addition of magnets, the density of plasma is increased and so is the deposition rates[37]. It also helps preventing the substrate from being damaged by the direct impact of these electrons.

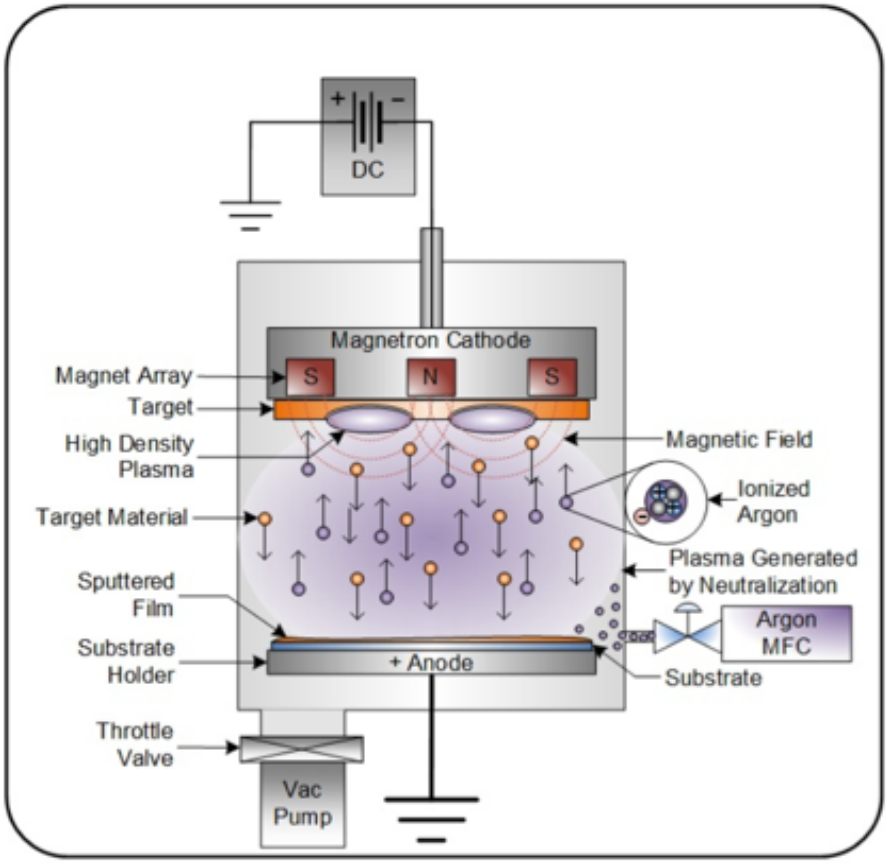

Figure 3.5 Diagram of the DC magnetron sputtering process [36].

DC sputtering is extensively used in semiconductor industry for the fabrication of microchip circuitry. Since the thermal evaporation of source material is not necessary, nearly all materials can be deposited by this technique regardless of their melting temperature. Other advantages over evaporation include but not limited to better step coverage, suitable for compound or alloy deposition, less waste of target material (considerable materials are deposited on chamber walls in evaporation), and better uniformity and thickness control of deposited film. The primary limitation of DC sputtering is that over time the charge buildup for non-conducting insulating materials can result in arcing or even complete failure of process. However, this could be overcome by using the radio frequency (RF) sputtering where alternating the electrical charge prevents the accumulation of charge on the target as well as the coating material.

3.2.3 Low Pressure Chemical Vapor Deposition (LPCVD)

Different from evaporation and sputtering discussed above, low pressure chemical vapor deposition is a chemical deposition technique to produce high purity films in the semiconductor industry, especially for the deposition of polysilicon thin films. In LPCVD, reactive precursor gas is introduced into a hot walled tube with a pressure ranging from 10-1000 mTorr; at the proper temperature, the decomposition of gas absorbed on substrate surface is triggered and forms the solid phase materials, with excess gas and volatile by-products pumped out of the tube. An example of thermal decomposition is:

Pyrolysis $$AB(gas) \rightarrow A(solid) + B(gas) \quad (3.1)$$

a-Si at 650℃ $$SiH_4(gas) = Si(solid) + 2H_2(gas) \quad (3.2)$$

As shown in Fig. 3.6[38], at low pressure, chemical reaction rate is lower than gas arriving rate, and the deposition rate then primarily depends on the temperature of substrate. Because of

that, substrates to be coated can be vertically stacked close to each other without degradation of uniformity as long as the temperature is well controlled. Multiple heaters are commonly used for LPCVD in order to achieve a uniform distribution of temperature above 500 ℃ inside the chamber and on the wafer boat.

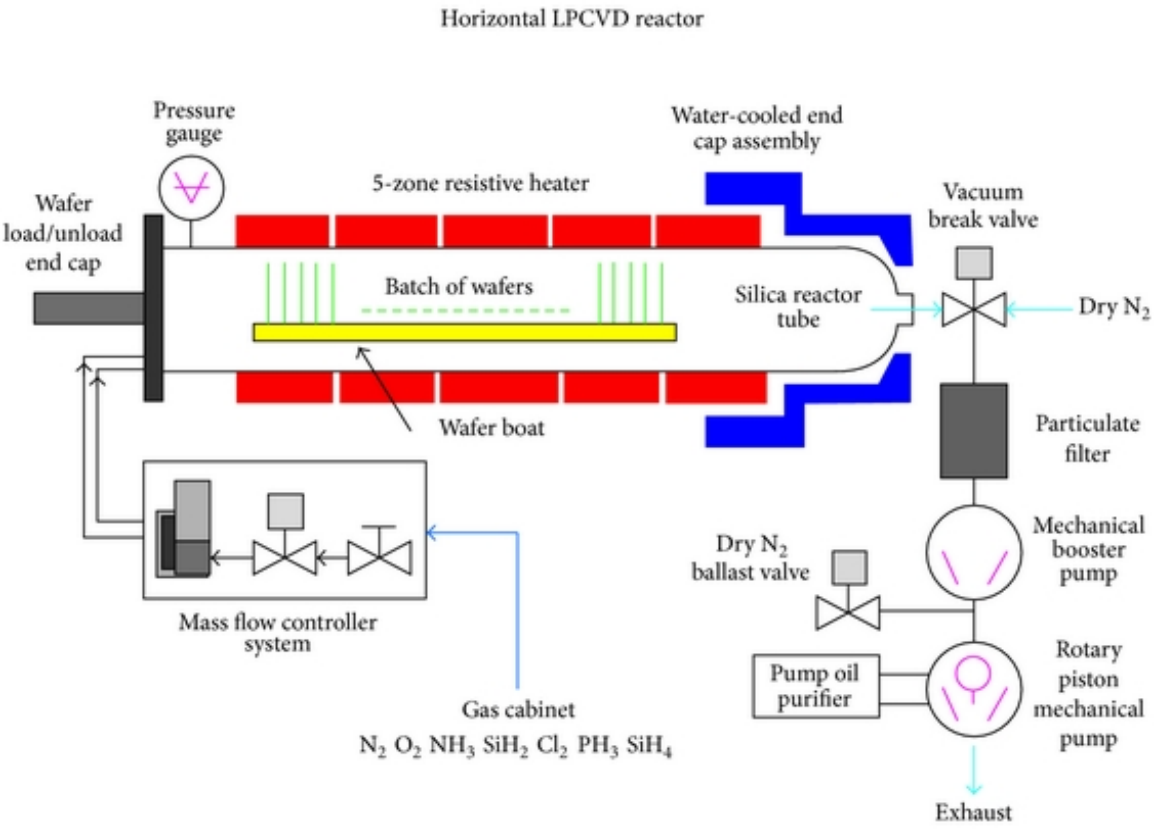

Figure 3.6 Schematic of a LPCVD system with the silica reactor tube [38].

There are also other chemical vapor deposition techniques in which the decomposition of precursors is achieved by different means, such as plasma enhanced chemical vapor deposition (PECVD) and atmospheric pressure chemical vapor deposition (APCVD). However, LPCVD is still a preferable technique for its excellent uniformity of thickness and purity, and simplicity of processing batch wafers.

3.3 Etching

Etching is a critically significant subtractive process in nanofabrication. By doing etching, materials are selectively removed to make the pattern emerge after lithography, transferring the existing pattern to the underneath material or cleaning the surface.

People are generally interested in three properties which characterize an etching process. The first is the etch rate; the depth of etching can be estimated by the total etching time when the etch rate is known. The second is the selectivity, which describes the ability of the etching agent to remove one certain type of material without damaging the others. Etching selectivity is therefore described by the ratio of the etching rate between different materials. The difference in etching result of a film is shown in Fig. 3.7, with film on the left etched with high selectivity and on the right low selectivity.

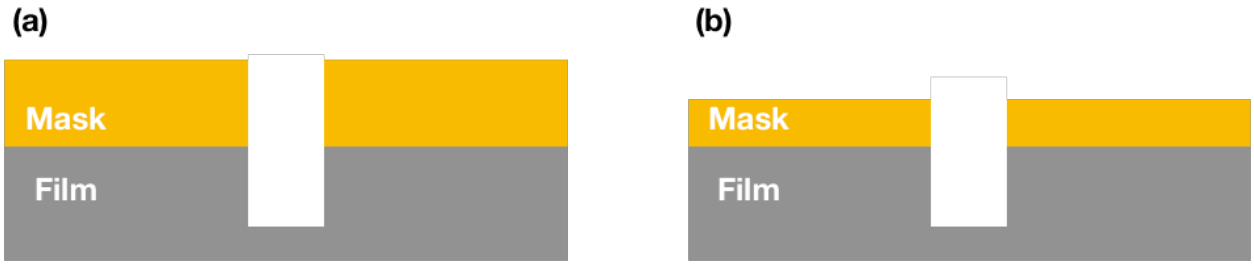

Figure 3.7 An example of etching of the film with (a) high selectivity where the film is etched while the mask on top remains undamaged; (b) low selectivity where both film and mask are attacked.

The third is the property of anisotropy. Ideally, etching is supposed to precisely transfer the mask pattern at the exact dimensions, but distortions are inevitable in practice. Anisotropic etching features different etch rates in the vertical and lateral directions, while in isotropic etching the rate is the same in all directions. The degree of anisotropy is defined by

$$A = 1 - R_L/R_V \tag{3.3}$$

where R_L and R_V are the lateral and vertical etch rates, respectively. Fig. 3.8 illustrates different degrees of anisotropy in an etching process[39].

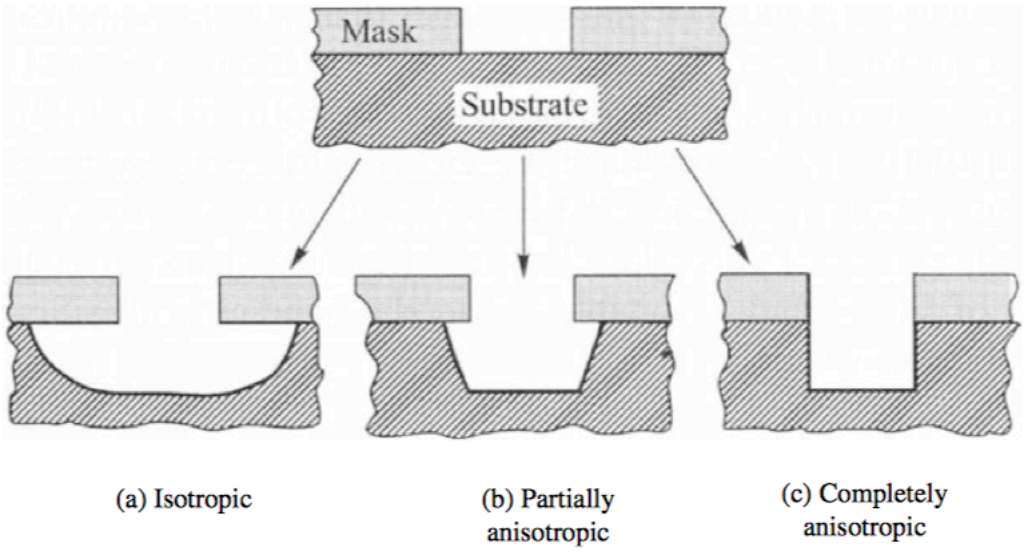

Figure 3.8 Schematic of (a) isotropic, (b) partially anisotropic, and (c) completely anisotropic etching[35].

Etching techniques can be categorized into two groups according to the phase of etchants: wet etching uses liquid-phase etchants, whereas dry etching uses gas-phase etchants.

3.3.1 Wet Etching

Wet chemical etching, also known as wet etching, is a low-cost etching technique that widely used in micro- and nano- fabrication. The entire wet etching process involves multiple chemical and physical sub-processes, which are illustrated in Fig. 3.9. The liquid etchant is first transported to the surface of substrates by means of diffusion, followed by the chemical reaction with the materials to be removed at the exposed sites. Soluble by-products from the reaction is then desorbed and removed by diffusion.

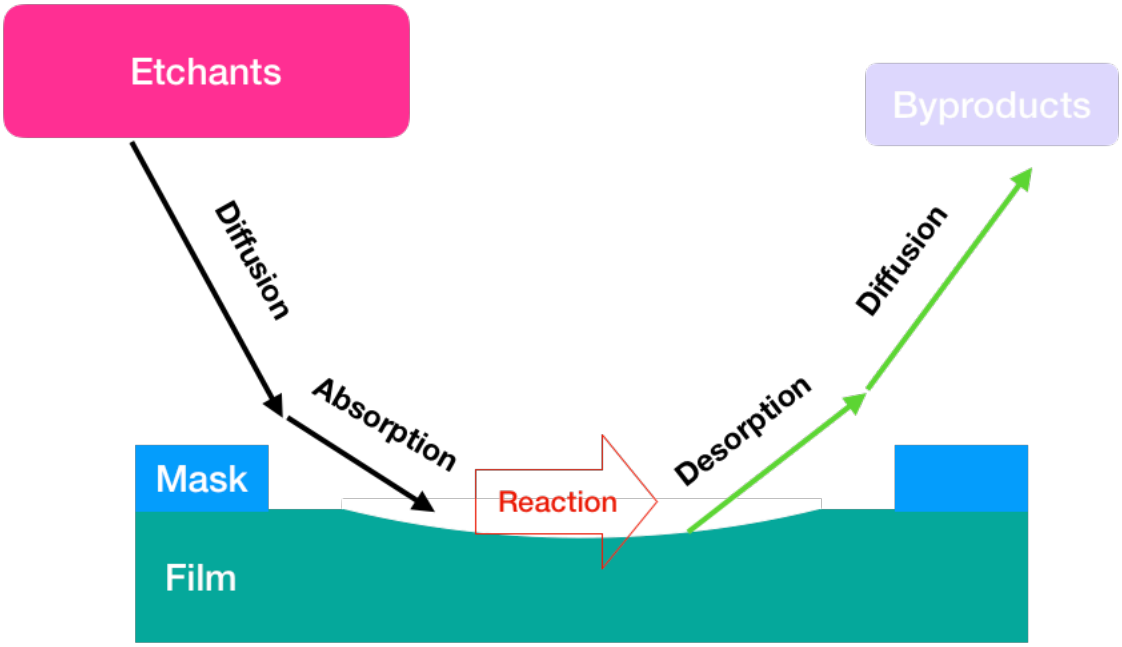

Figure 3.9 Mechanisms of a wet chemical etching process.

Wet etching is generally isotropic, which means etching takes place both laterally and vertically. The liquid-phase reactive agent can easily etch underneath the mask, resulting in the dimension loss during the pattern transfer step. For this reason, wet etching is barely used for high resolution patterning.

3.3.1 Plasma Etching

Plasma is highly conductive, partially ionized gas comprised of equal numbers of positive and negative charge, and some neutral molecules. Plasma can be artificially generated by heating or applying strong electromagnetic field at low pressure, which will break down some of the gas molecules and generate electrons, ions, free radicals and photons. Plasma etching is one subset of dry etching since no liquid-phase agent is involved.

Plasma etching is a highly versatile technique that can provide isotropic or anisotropic etch profiles, and is preferred for high resolution fabrication due to the ability of faithful pattern transfer

into underlying layers. The plasma etching process is quite similar to the DC and RF sputtering discussed in the previous section, expect that almost all plasma etching uses RF power source. When frequencies are above 50 kHz, the ions are not capable of following the switching due to the heavy mass. However, electrons have much smaller mass and can directly gain energy from the RF field, and the oscillating high energy electrons effectively facilitate the ionization of the gas. Another advantage of RF source is electrons would significantly eliminate the positive charge buildup during each half cycle. Fig. 3.10[40] shows the potential distribution for the parallel plate RF plasma. The part with a fixed potential V_P is the glow region, where recombination of excited ions and electrons lead to bright light emission; within this region plasma is highly conductive due to fast electrons. Voltage drop occurs at the two ends where electrons are lost to the electrodes. Overall, the plasma is always positively biased with respect to both cathode and anode, with V_P near the grounded anode and $V_P + V_{DC}$ (V_{DC} is the applied voltage) at the cathode. The sputtering technique discussed in Section 3.2.2 takes advantage of this mechanism to initiate sputtering at the cathode and achieve the deposition at anode, whereas in plasma etching only the removal of materials at the cathode is concerned.

If only noble gas (usually argon) is present in the reaction chamber, the dry etching proceeds is solely physical: substrate atoms are dislodged when the energy gain during collision exceeds the bonding energy. Unlike wet chemical etching, physical dry etching (also named sputtering etching) is highly directional and non-selective. However, the reaction relies on the physical bombardment between ions and atoms is not efficient, non-volatile product also raise the problem of re-deposition on the wafers to be etched.

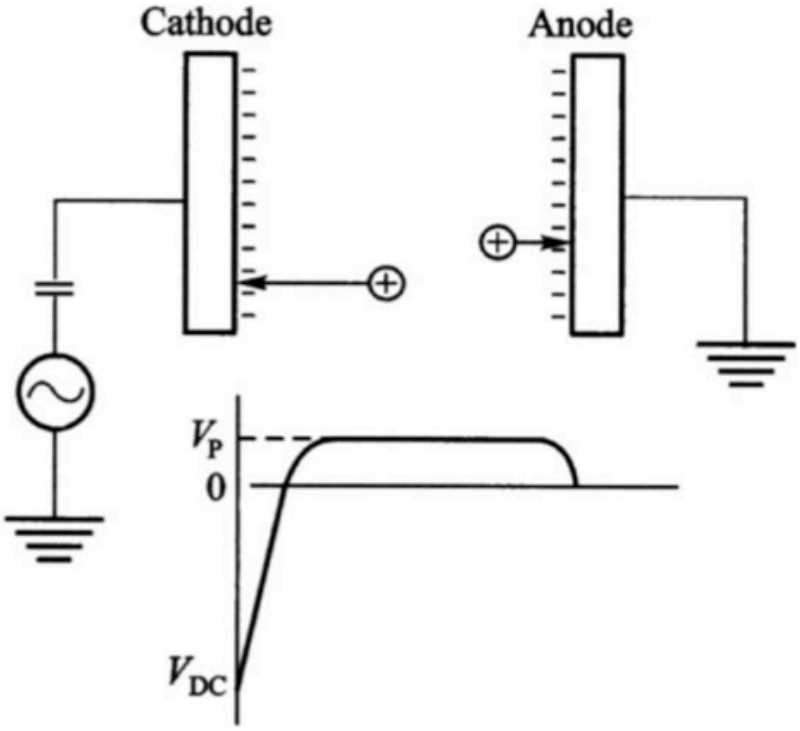

Figure 3.10 A parallel plate RF plasma system and its potential distribution [40].

Reactive ion etching (RIE) is an ion enhanced etching technique and is the most widely used pattern transfer technique in modern nanofabrication. In fact, RIE is commonly referred to as "dry etching", even though dry etching is a much broader category including various techniques with RIE as only one of them. Different from the sputtering etching where only noble gas is used, in RIE reactive gas is introduced so that both physical and chemical reactions take place, which greatly increase the etching rate and the etching selectivity.

The whole RIE process can be divided into 3 simultaneous sub-processes illustrated in Fig. 3.11[41-43]:

(1) Ion with high kinetic energy impact the substrate surface, creating a fresh surface free of native oxide layer and contaminant. This will promote the surface absorption of reactive radicals. Physical sputtering takes place so that part of the material is removed from

surface, meanwhile the sputtering process can physically damage and weaken the chemical bond of the material.

(2) If the ions are reactive they can also react with material atoms directly, forming volatile products which leave the substrate by diffusion.

(3) Free radicals generated in plasma diffuse to the substrate surface (thus non-directional). The radicals are able to move around the surface before absorbed and react with the material. Volatile compounds leave the surface and are then pumped out.

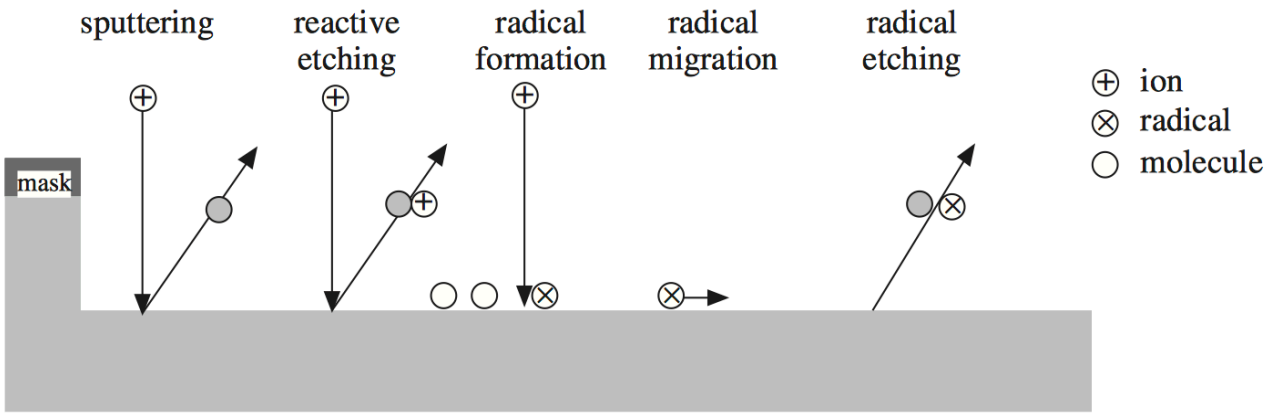

Figure 3.11 Processes on the surface of material during reactive ion etching [41].

In fact, the physical process of sputtering doesn't contribute significantly to the etch rate by knocking out atoms, mostly because of the very rare presence of ions. However, ion bombardment is still of great importance for realizing anisotropic etch with RIE because it causes structural damage such as dangling bonds and dislocations, the horizontal surface is therefore more reactive than the sidewall which is less impacted by ions. As a result, the chemical etching by neutral radicals is increased. Fig. 3.12 compares the etch rate of silicon by three different dry etch methods: pure chemical dry etching (PE), reactive ion enhanced etching (RIE), pure physical ion beam

etching (IBE). Chemical etch with ion assistance is clearly more efficient than the other two techniques.

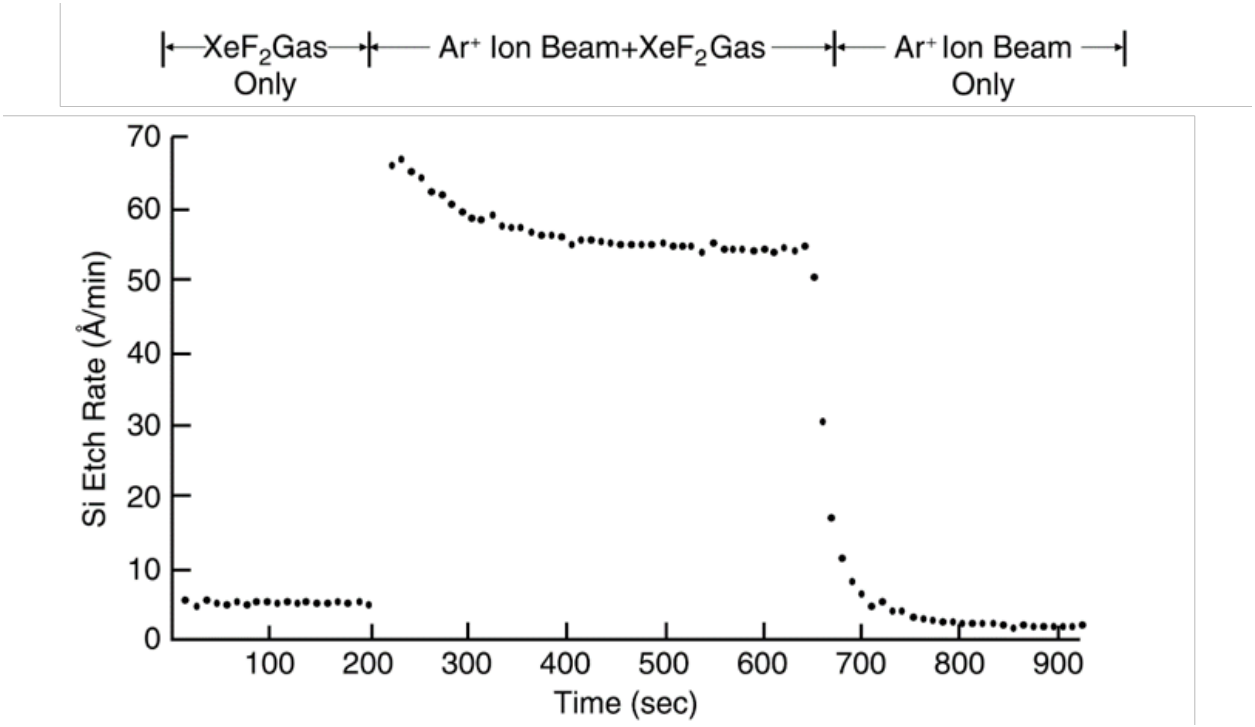

Figure 3.12 The etch rate of silicon by XeF_2 gas only, Ar plasma + XeF_2 gas, and Ar plasma only [42].

Another mechanism for anisotropy in RIE is the removal of passivation layer by ion bombardment. Halogen compounds are the mostly used gases in RIE for inorganic and metallic materials, but their radical etching can be easily stopped by polymers. This provides a route to prevent lateral etching on the sidewalls. When gas such as CHF_3 is added to the plasma, the carbon compounds can be deposited on both the sidewalls and the horizontal surface as passivation layer. While isotropic chemical etching is stopped by the passivation film on sidewalls, at the bottom the directional ion bombardment effectively removes the passivation and the progress of etching proceeds vertically[44]. Figure 3.13[45] gives typical etch profile by three different dry etching techniques including reactive ion etching. IBE features low selectivity and etch rates, and produces

positively tapered profiles, with chemical PE gives very high selectivity and etch rates, leading to isotropic undercuts. RIE enables a flexible profile control without much compromise on the etch rate and selectivity.

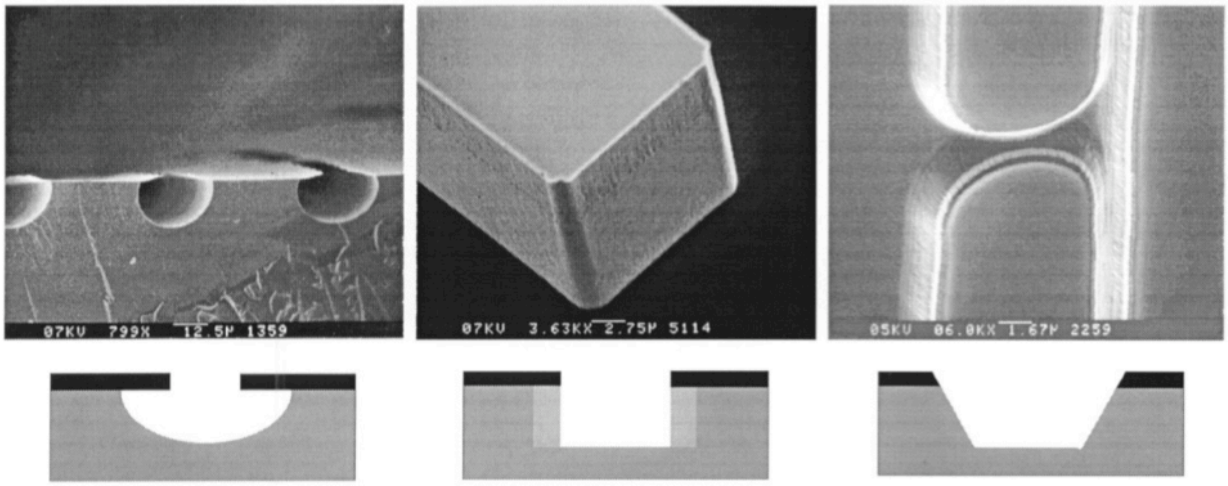

Figure 3.13 Typical etch profiles by chemical PE, RIE and IBE (left to right) [45].

The need for high etch rate drives the development of RIE systems. The etch rate depends on the density of plasmas (ions and free radicals altogether). In conventional RIE with parallel plate setup, an increased RF power will increase the plasma density. According to Fig. 3.10 this also leads to a higher bias voltage at cathode and thus enhance the physical sputtering. As a result, the etch selectivity deteriorates. To address this issue, high density plasma systems (HDP) with independent control of ion bombardment energy and plasma density are designed.

Inductively coupled plasma systems (ICP-RIE) is the most popular HDP system. As depicted in Fig. 3.13[46], an additional radio frequency power is applied to the induction coil outside the chamber, which facilitate the cycling movement of charged particles. Density of plasma is therefore increased due to the increased ionization probability. Another RF source connected to the stage is primarily used to control the bias voltage, which determines the ion energy. By

separating the ionization and ion bombardment, high plasma density and high etch selectivity can be achieved at the same time.

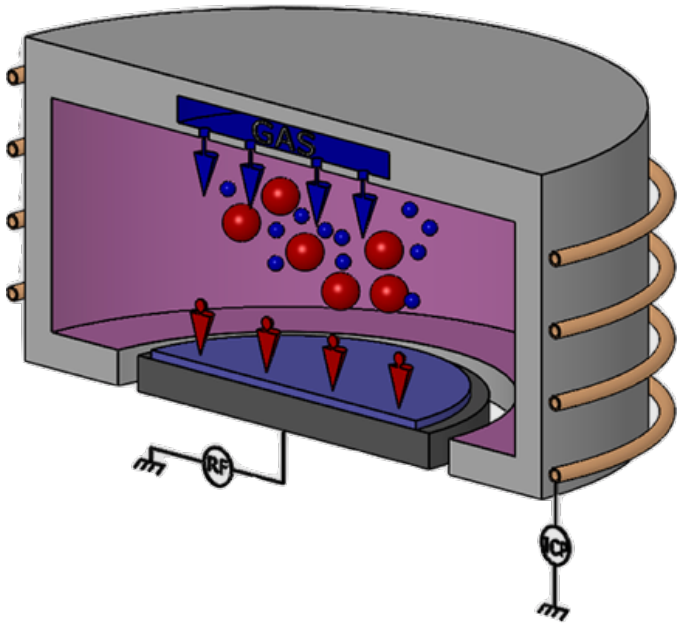

Figure 3.14 Schematic of inductive coupling plasma setup [46].

The rapid development of semiconductor processing significantly raise the requirements of selectivity, control of profile and etch uniformity[47]. Plasma etching, especially RIE systems, perfectly suits the needs of achieving faithful pattern transfer in high resolution lithography. However, reactive ion etching is a rather complicated process and currently there are no theories available to describe the whole RIE process[48]. In practice the pattern transfer by RIE is usually carried out on an experimental and empirical basis.

Reactive ion etching also plays an important role in the fabrication of subwavelength moth-eye structures. Fig. 3.14[49] shows the pictures of several typical artificial MEAR surface. It is obvious that the feature size of moth-eye nanostructures is quite small. With a small pitch and high

aspect ratio, etching for such structure should be anisotropic and highly selective. By considering all these restrictions, RIE is almost the only remaining candidates.

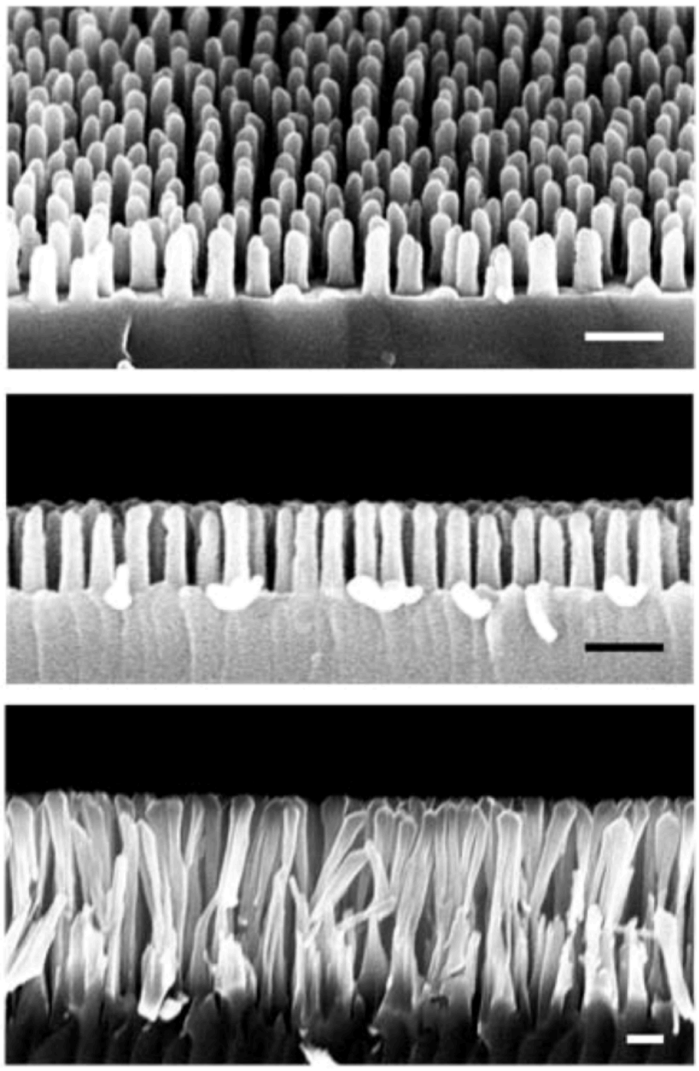

Figure 3.15 Scanning electron images of two different nanopillar arrays: tilted top view (top image) and sideview (middle image) of 350-nm-tall pillars; sideview of 1400-nm-tall pillars (bottom image). Scale bar: 200 nm [49].

Chapter 4 Fabrication Process of Moth-Eye Anti-Reflective Structures on Glass

This chapter focus on the fabrication process of the MEAR treated surface on the glass. A novel and scalable fabrication method suitable for space applications is proposed that makes MEAR accessible to the CubeSats developers. In our process, instead of direct etching into the glass, the desired structures are fabricated with poly-silicon which is deposited on the glass substrate. By a combination of nanosphere lithography and reactive ion etching of silicon with tapered sidewall control, the patterned silicon moth-eye pillars undergo an atmospheric oxidation procedure to convert the opaque Si into transparent SiO2.

4.1 Nanosphere Lithography

In a top-down fabrication process for moth-eye surfaces, there are various techniques available to create nano-scale moth-eye features with a hexagonally closed packed arrangement. Approaches such as electron-beam lithography[50-52], direct laser ablation[53], interference lithography[8, 54] and anodized aluminum oxide[55] have all been proven capable of producing two-dimensional moth-eye nanopillar arrays on a variety of substrate materials. Among above methods, electron beam lithography is largely favored due to the straightforward and precise control over the size, spacing, and shape of nanostructures[56]. However, the process for that is complex and the throughput is rather limited due to the lengthy writing time. The cost in the case of e-beam lithography to cover the surface area of solar cell would be considerably expensive. To overcome the drawbacks such as high cost, complex equipment set-up and poor flexibility in

defining patterns associated with the methods above, nanosphere lithography has been proposed and developed.

4.1.1 Template Deposition

First reported by Fischer et al.[57], nanosphere lithography (NSL) , also known as colloidal lithography (CL) , is an emerging technique that enables the formation of hexagonal close-packed (HCP) or non-close paced (HNCP) pattern by the self-assembly of colloid particles. Modern synthetic technology is able to produce colloid particles such as polystyrene (PS) or silica beads with a very narrow size distribution in the range from 100 nm to 1 μm[58]. Although the spacing of the colloid template is determined by the bead diameter, with proper post-treatment such as material deposition, reactive ion etching , annealing and ion milling, the actual feature size made from the template can vary from ten to several hundred nanometers[59].

2D hexagonally ordered templates can be fabricated by NSL via various strategies. Fig. 4.1 describes some available deposition strategies, including drop-coating, spin-coating, Langmuir-

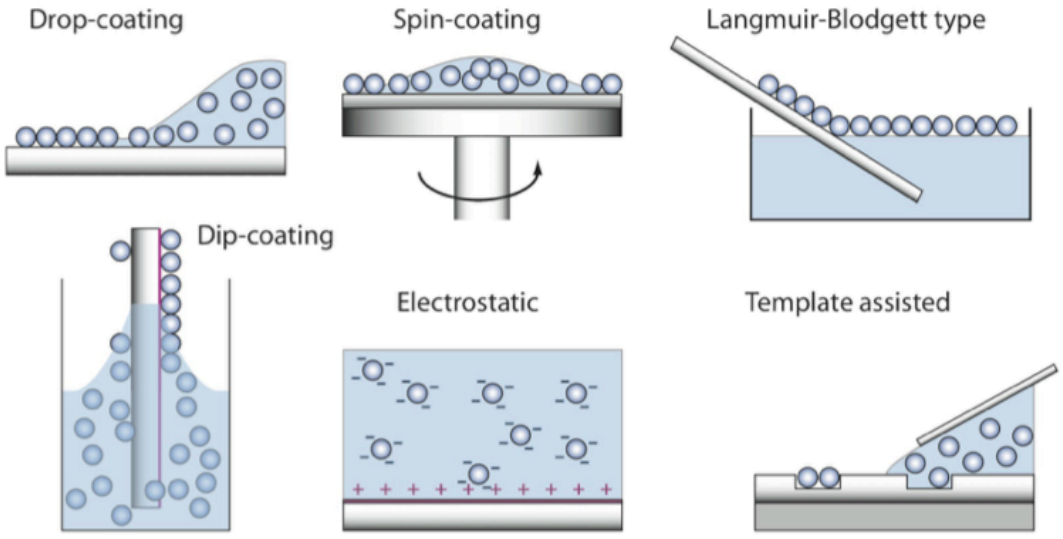

Figure 4.1 Several example nano-beads deposition strategies [59].

Blodgett type, dip-coating, electrostatic guided coating and template assisted coating[59]. Comprehensive review on the nanosphere synthesis, self-assembly mechanism, post deposition modification for different applications can be found elsewhere in the references[56, 58-60].

By comparing the merits of each deposition strategies, it was determined that a Langmuir-Blodgett (LB) deposition should be performed for the fabrication of moth-eye template because of the following reasons. The LB technique can produce large area of naturally HCP colloidal monolayers on different types of substrate materials in a safe and repeatable manner. It is also an easy to perform process that relatively little training is needed for a successful deposition. In addition, the LB technique features considerably low-cost as no particular equipment is needed for a low-volume laboratory-scale production, in fact, only a water bath would be sufficient. Last but not least, it is also a scalable technique that modular Langmuir-Blodgett trough with high throughput and precise quality control of film is commercially available.

Following the deposition technique introduced in references[13, 15, 61], a simplified LB-type dip-coating process can be implemented to form the HCP monolayer of polystyrene nanosphere on the glass substrate as depicted in Fig. 4.2. First, a de-ionized water bath is prepared with the substrate immersed at the bottom. Two small chunks of metal are then used as stoppers to prevent the substrate from movement during operation and also provide a tilted angle for the ease of picking up the substrate before finishing. By dropping colloid on a tilted hydrophilic glass slide that is partially immersed, self-assembly of the nano-beads takes place[15]. Colloid particles are trapped at the air-liquid interface due to the electrostatic and capillary forces, leading to domains of HCP monolayer dispersing across the surface of water. With the addition of surfactant, the free-floating monolayer domains are expected to be pushed together, constituting a mono-layer area of HCP film that is sufficient to cover the area of glass substrate. Once such film is formed over the

top of underlying substrate, the glass slide is gently removed and the substrate immersed can then be slowly lifted upwards with the HCP film precipitated on it. At the end of deposition process, the backside of the substrate is cleaned to remove any residual particles and finally the glass substrate is left at a small incline to facilitate the fluid flow driven by gravity.

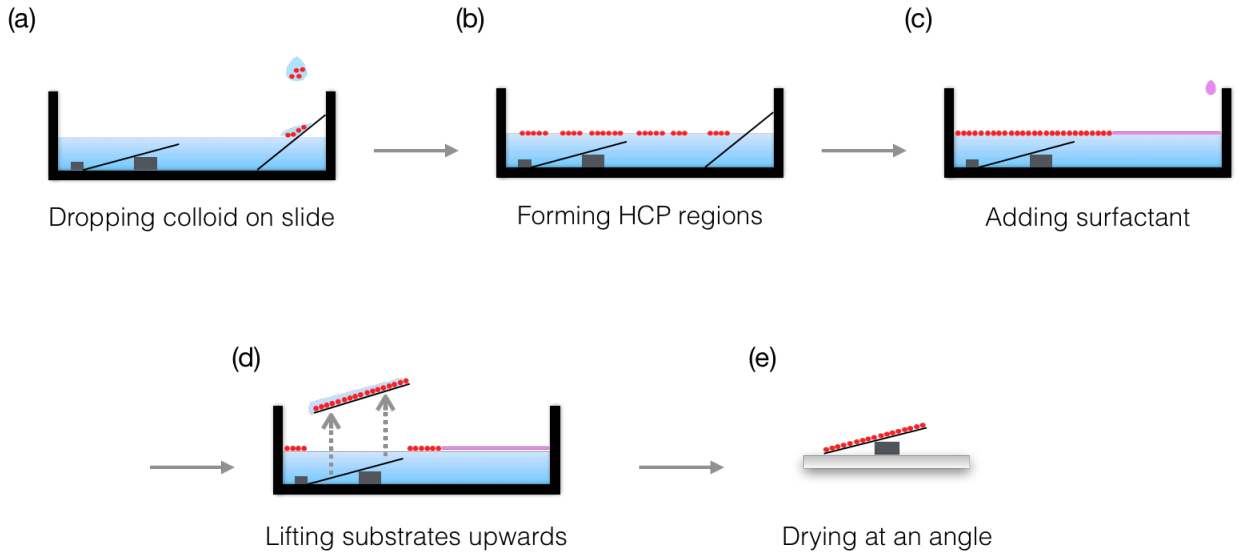

Figure 4.2 Process flow illustrating the colloid deposition process for making the initial template: (a) dropping colloids on tilted glass slide; (b) forming HCP regions by self-assembly; (c) introducing surfactant (Sodium Dodecyl Sulfate); (d) lifting the substrates located at the bottom; (e) finishing deposition by the evaporation of liquid[13, 15, 61].

For our process, the glass substrate underwent a short plasma treatment before being mounted on the metal stoppers at the bottom of the water bath for an increased surface energy[62]. Oxygen plasma at 100 mTorr with 50 Watts RF power was implemented for 1 minute, not only to remove organic contamination, more importantly, to terminate the treated surface with hydroxyl groups (-OH) so that the surface's wettability and adhesion to other coatings would be enhanced. This step is quite advantageous for a successful transfer of self-assembly nano-bead onto the substrate; moreover, the dip coating should be carried out right after the surface modification of glass

substrate because the plasma-treated surfaces may recover their untreated characteristics with prolonged exposure to the air[63].

Fig. 4.3 compares the behaviors of a wetting and de-wetting colloidal suspension respectively[59]. For wetting suspension, HCP monolayer will be left on the surface once the thickness of water film falls below nano-beads' diameter, while keeping their arrangement. In comparison, de-wetting suspension forms droplets on the substrate surface that will not spread out because of the high contact angle, resulting in the convective flow of the nano-beads contained inside that will destroy their arrangement. Although this is an unwanted process in our case, the opposite behaviors of suspension are crucial for a guided deposition of beads, for instance the local deposition of beads, in which deposition is initialized only within hydrophilic treated regions of the surface and prevented at hydrophobic regions[64].

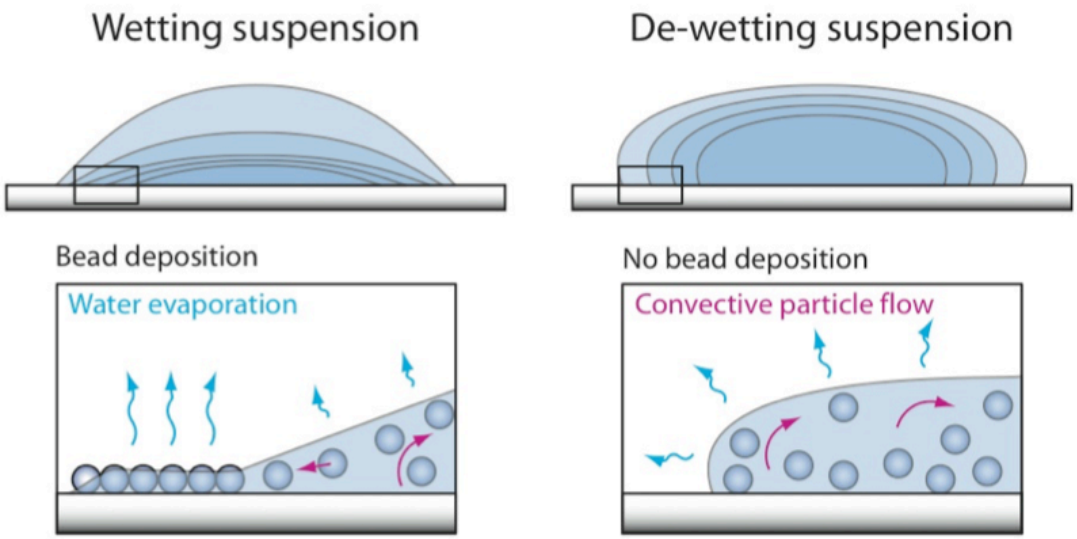

Figure 4.3 Behaviors of colloidal suspension on wetting and de-wetting surfaces [59].

To produce the template, a 2.5-litre borosilicate glass dish partially filled with DI water was used for the water bath. Substrates after plasma treatment was then mounted on the metal chunks

at the bottom. A microscopic glass slide was partially immersed close to the sidewall of water bath at an incline of 40°, using as a ramp for the addition of colloid drops. Uniform polystyrene (PS) latex nanosphere suspension of 10% w/v (200 nm-diameter, MagSphere Inc.) was mixed with ethanol at 1:1 ratio[61], and dispensed on the tilted slide via 10 μL calibrated micropipette at a speed around 2 $\mu L/sec$. It was found that when the suspension to ethanol ratio was fixed, the way that the PS nanosphere organized on water surface is influenced by the angle between glass slide and the surface of water (shown in Fig. 4.4[13]), largely because of the flow speed of colloid drops entering the water surface. However, in practice there are no clear boundaries for the angle range of slide and the resulting dispersal regimes, and a moderate angle of 40° can give high quality monolayer and was therefore chosen for our experiment.

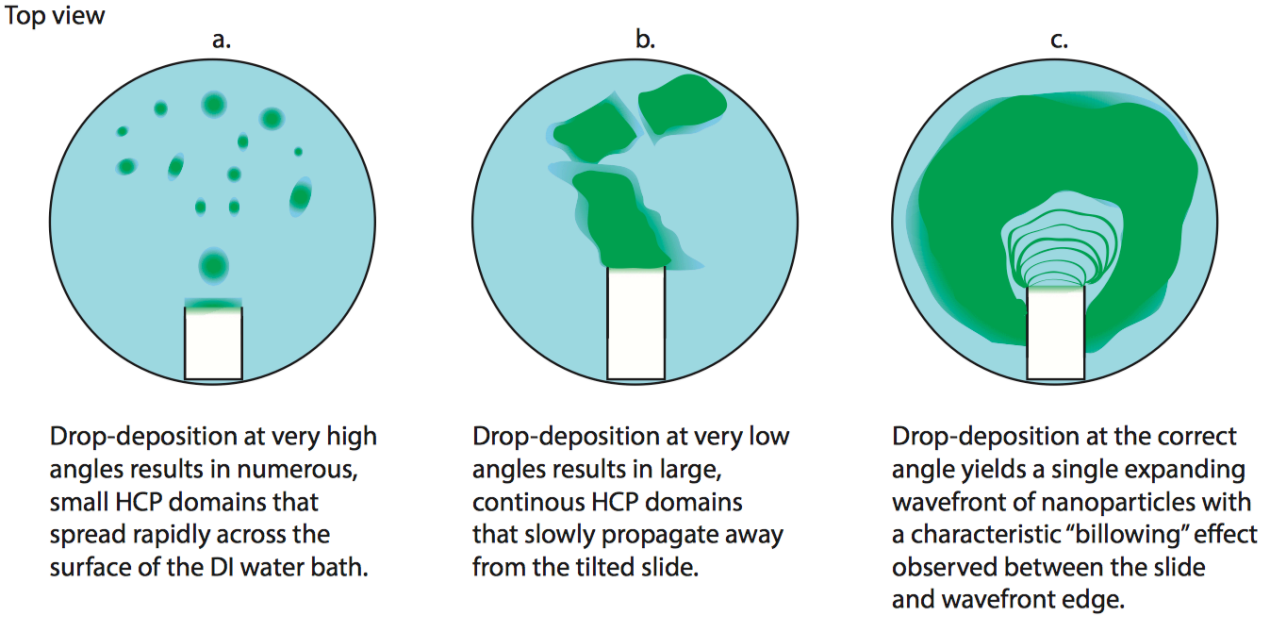

Figure 4.4 Birds-eye view observation on different colloid dispersal regimes with respect to the angle of tilted glass slide [13].

After the formation of monolayer on the air-water interface and the removal of glass slide, surfactant--sodium dodecyl sulfate solution (10%, Fisher Scientific) was then dropped at the

surface of water. The added surfactant will occupy the interfacial region towards the maximum coverage[65] and thus compress the gaps between monolayer domains to constitute a single uniform monolayer. Following this, substrate was lifted up at an angle by a pair of offset thumb forceps slowly through the air-water interface, leaving the water bath together with the HCP nanosphere monolayer and small amount of water. Finally, the substrate was covered by a uniform PS-sphere monolayer with HCP arrangement after drying in a ventilated wet bench. The SEM micrograph of the coated 2-dimentioanl HCP monolayer is shown in Fig. 4.5.

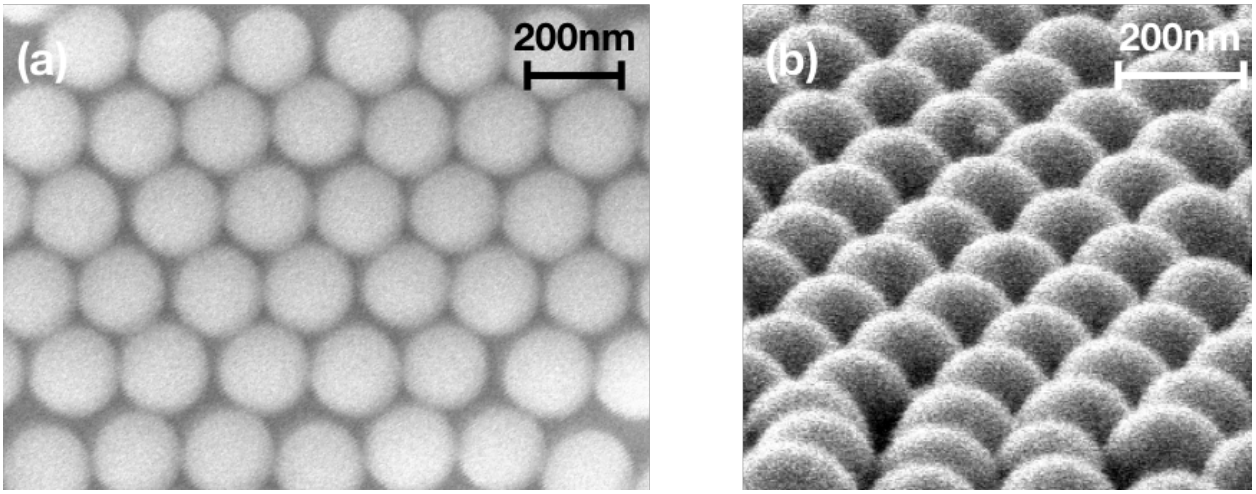

Figure 4.5 (a) Birds-eye view and (b) 70° tilted view SEM images of the 2-dimentional HCP array coated by the LB-technique.

For a simplified process as reported above, although the construction of large area defect-free PS nanosphere doesn't involve expensive and sophisticated instrument, the quality of the coated film is still affected by a number of factors: de-wetting substrates, un-even flow rate during colloid dropping, inappropriate tilted angles of glass slide or unstable movement when lifting up the substrates, which can result in the degradation of self-assembly process. Example of an un-uniform nanosphere arrangement transferred on the substrate is shown in Fig. 4.6, with (a) featuring a multilayer structure and (b) a poor coverage of the substrate surface. Despite all these operational

considerations, the LB-technique is overall a straightforward, safe and effective nano-bead deposition method that can organize the HCP self-assembly monolayer on a variety of substrates materials, which makes it a favorable approach to create the template for MEAR structure fabrication.

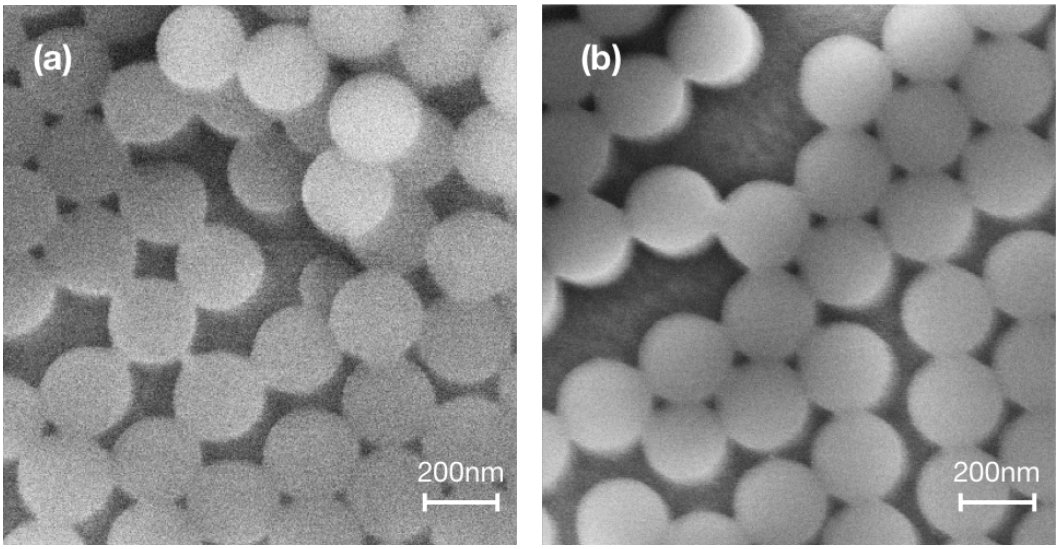

Figure 4.6 SEM images illustrating two typical defects on the substrate, with (a) formation of multi-stacked nanospheres and (b) insufficient coverage of non-closed packed PS nanosphere monolayer.

4.1.2 Modification of Polystyrene Arrays

Nanosphere lithography is a cost effective and versatile technique for producing defect-free template with periodic arrangement. Fig. 4.7 gives examples of different structures formed by nanosphere lithography[66, 67]. By directly using the colloidal arrays as etching or deposition masks, faithful nano-patterning of periodic triangular and spherical shape are enabled. However, there is a distinct disadvantage of NCL compared to the conventional lithographic techniques that the resulting patterned shape is quite limited to either triangular or spherical if the template is directly used as the processing mask. To address this issue, modification of the colloid mask is

developed such that the shape and size of the particles can be intentionally modified by proper post-treatment.

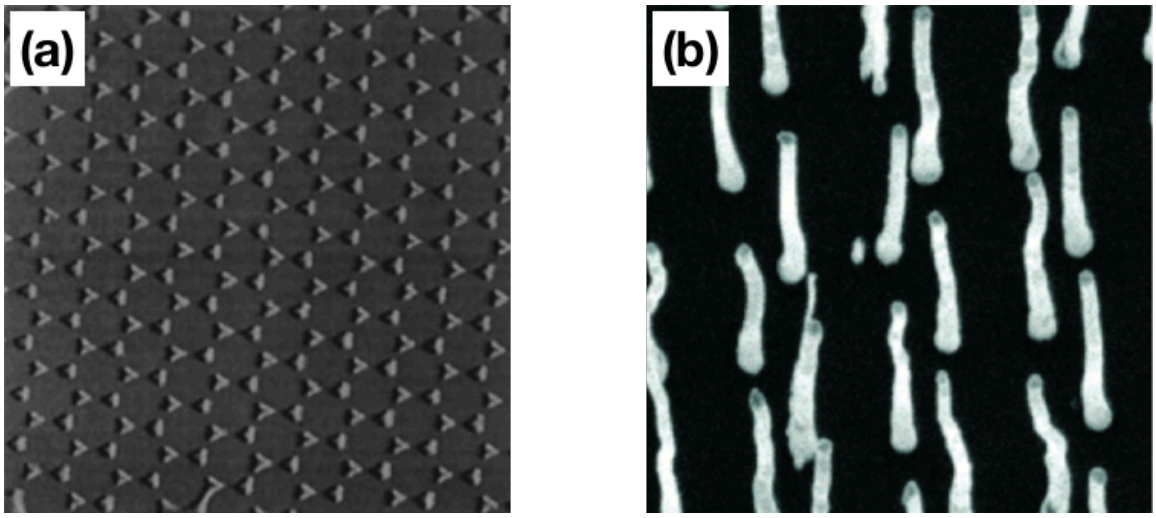

Figure 4.7 Examples of structures formed by nanosphere lithography: (a) triangular metal dot array [66]; (b) vertically aligned carbon nanotube array [67].

In the fabrication of MEAR structures using PS nanosphere as mask, the pitch Λ of the pillar array is determined by the center to center distance of the latex spheres, which is also the initial diameter of closed packed nanobeads. Therefore, the pitch of biomimetic moth-eye pillar arrays is a fixed value once sphere of a certain diameter is chosen for the process. The shape of individual pillar, however, depends on the exact size of masking spheres during etching step and the way that etching proceeds.

Reactive ion etching is carried out to widen the gaps between individual PS nanospheres which were originally closed packed. Polymer spheres were etched for different time by oxygen plasma RIE at 20 Watts RF power, 20 mTorr pressure with continuous oxygen flow rate of 20 standard cubic centimeters per minute (sccm). The etch time by oxygen RIE ranges from 30 s to 120 s and the change in the sphere diameter was measured with scanning electron microscope. Fig.

4.8 compares the different size reduction results of spheres under O_2 RIE. It is obvious that as the distance between spheres increases with the etch time, the arrangement of coated monolayer becomes hexagonally non-closed packed (HNCP).

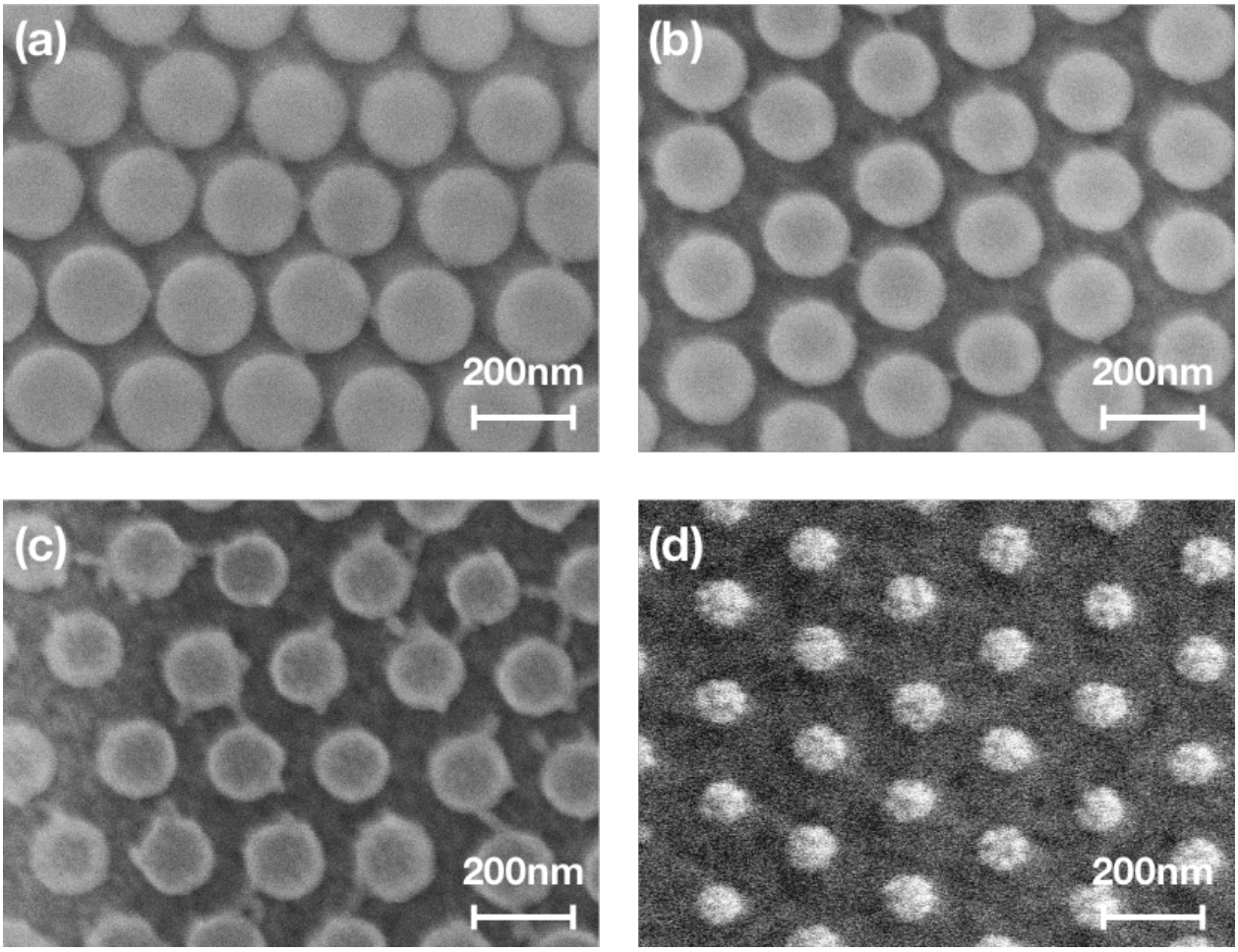

Figure 4.8 SEM images of PS latex nanosphere undergone O_2 plasma treatment for (a) 30s; (b) 40s; (c) 60s; (d) 80s.

Fig. 4.9 plots the PS nanosphere diameter as a function of the etch time measured with SEM, and gives a linear fit indicating an approximate reduction rate of diameter at 70 nm per minute. In our MEAR structured glass fabrication process, the PS latex spheres were treated by O_2 plasma for 40 s, resulting in a 23.3 nm radius reduction.

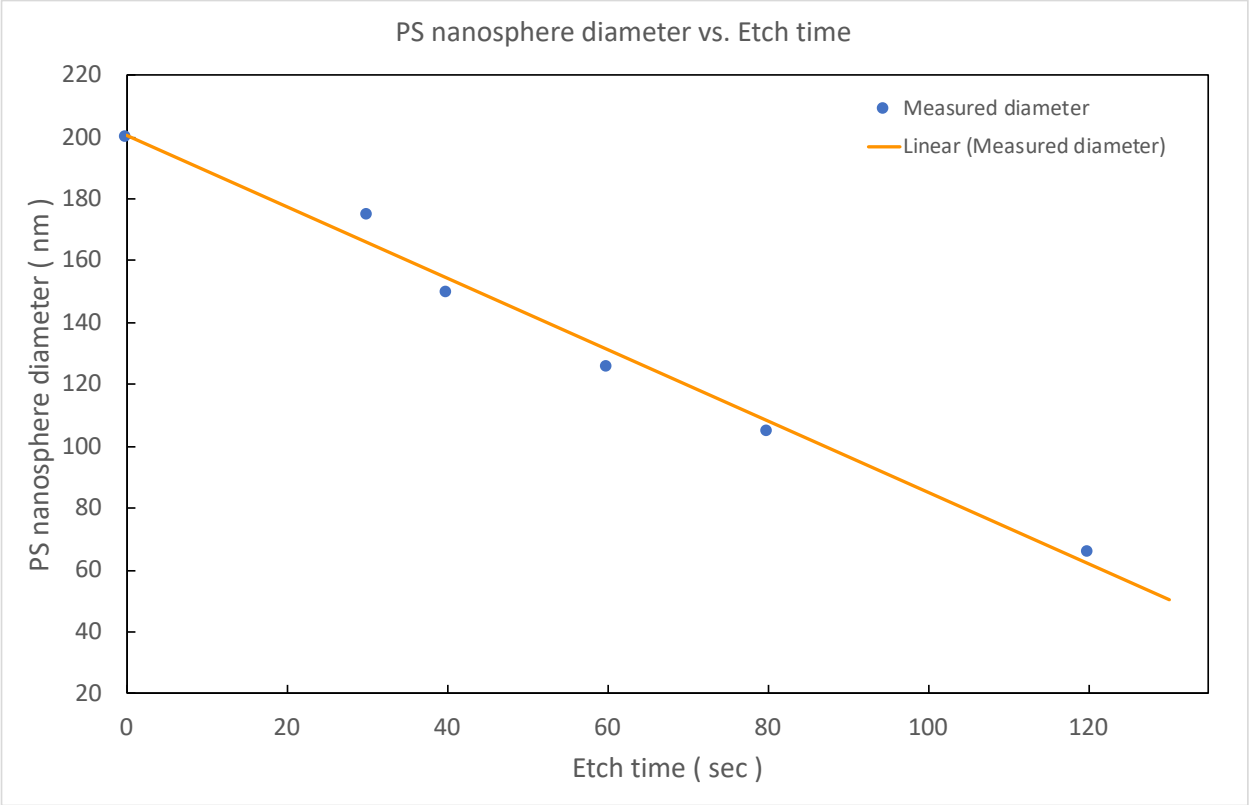

Figure 4.9 PS nanosphere diameter as a function of the etch time, fitting line gives an approximate reduction rate of diameter at 70 nm/min.

Following the size reduction of masking colloid particles by oxygen plasma, the influence of post-annealing on the etched PS nanosphere for MEAR structure fabrication was first investigated in our process. Generally speaking, polymers primarily consist of carbon chains and exhibit a glass transition above a certain temperature (T_g) due to the free-volume change[58, 68]. Polystyrene is a type of aromatic hydrocarbon polymer, and it also enters the melt state at elevated temperatures. The deformation of polymeric spheres above T_g has been utilized to produce gold disk arrays for the study of resultant plasmon excitations[69], in which the Au disk size could be controlled by changing the annealing condition since polymeric particles would spread horizontally with the increased annealing time. In our process, however, the annealing is performed not for changing the diameter of the PS nanosphere, but to achieve an increased contact area between masking

sphere and the substrate surface, which will positively affect the subsequent pattern transfer process from HNCP spheres to the material underneath.

Illustrative cross-sectional view of the PS nanosphere after three stages is given in Fig. 4.10, with dashed line showing the sphere border at the previous stage. During the anisotropic oxygen reactive ion etching, the part of sphere facing upwards is etched faster than the bottom, resulting in an irregularly shaped sphere as illustrated in Fig. 4.10 (b). Annealed under proper condition, the irregular sphere is expected to see deformation such that the lower bottom part in contact with the substrate first becomes glassy, resulting in a cap-like shape or jelly-like shape which has a much larger area in contact with the substrate while almost remaining the same diameter as that before deformation.

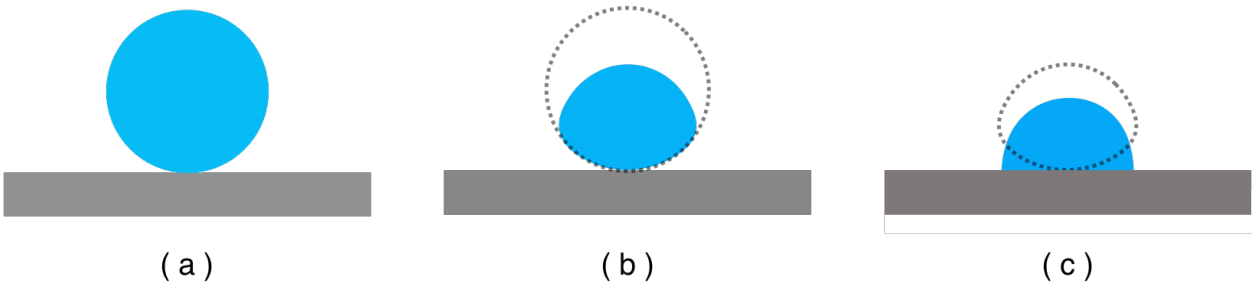

Figure 4.10 Schematics of the cross-sectional view of the PS nanosphere after different stages: (a) LB deposition on the substrate surface; (b) Oxygen plasma size reduction; (c) Annealing above glass transition temperature. Dashed line indicates the border of sphere at the previous stage.

In order to realize the partial deformation of polystyrene nanospheres without increase in its diameter, the temperature and time are both crucial parameters. For bulk PS films, the glass transition temperature is commonly considered to be about 373 K (100 ℃)[3]. However, the T_g value of PS micro- or nano- particles is quite controversial. Previous study reveals that depending on the synthetic techniques of the sphere, the glass transition temperature could be either identical

to[70, 71], or smaller than the bulk T_g value[72, 73], mostly because of the surface to volume ratio, density of packing and intermolecular entanglement. In consideration of the unusual thermal behavior, the annealing test of plasma treated PS nanospheres was carried out at temperature ranging from 90 ℃ to 170 ℃, for up to 15 minutes. It was found that for our self-assembly template, annealing at 130 ℃ for 5 minutes delivers the most favorable result.

Fig. 4.11 compares the profile of nanospheres before and after 5-min annealing at 130 degrees Celsius, with a 40 s oxygen RIE was performed before the thermal deformation. It was noticed that no drastic changes on the shape of PS nanospheres were discovered from the top view scanning electron microscopic images: a small decrease in the diameter of spheres of about 8 nm was measured; a minor improvement on the roundness of spheres was found. However, the change in the shape of sphere was still unclear.

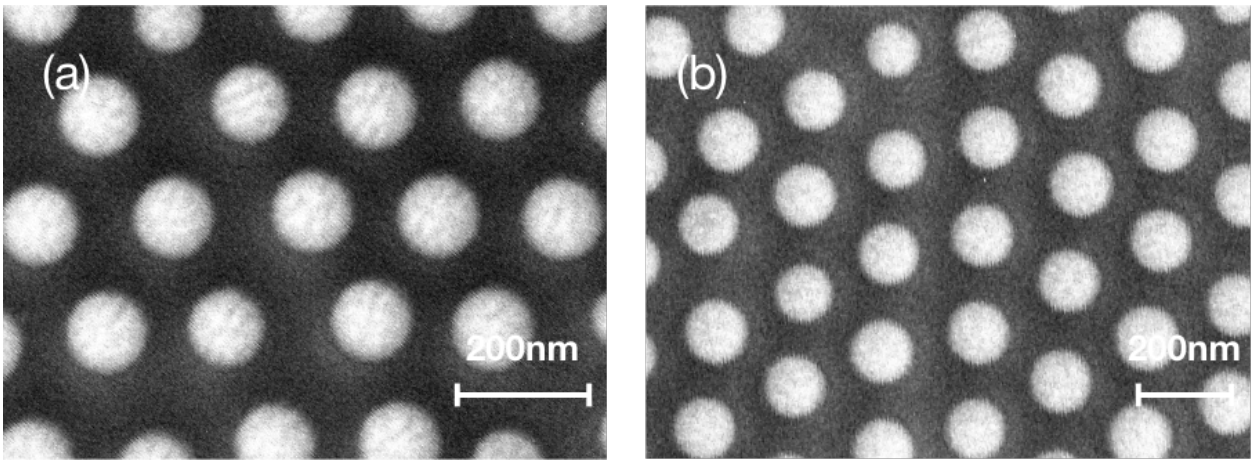

Figure 4.11 Top view SEM pictures of PS hncp nanospheres (a) before and (b) after annealing at 130 C° for 5 minutes.

Therefore, it was very necessary to take SEM at a tilted angle to investigate the thermal triggered deformation of polymer spheres, as shown in Fig. 4.12.

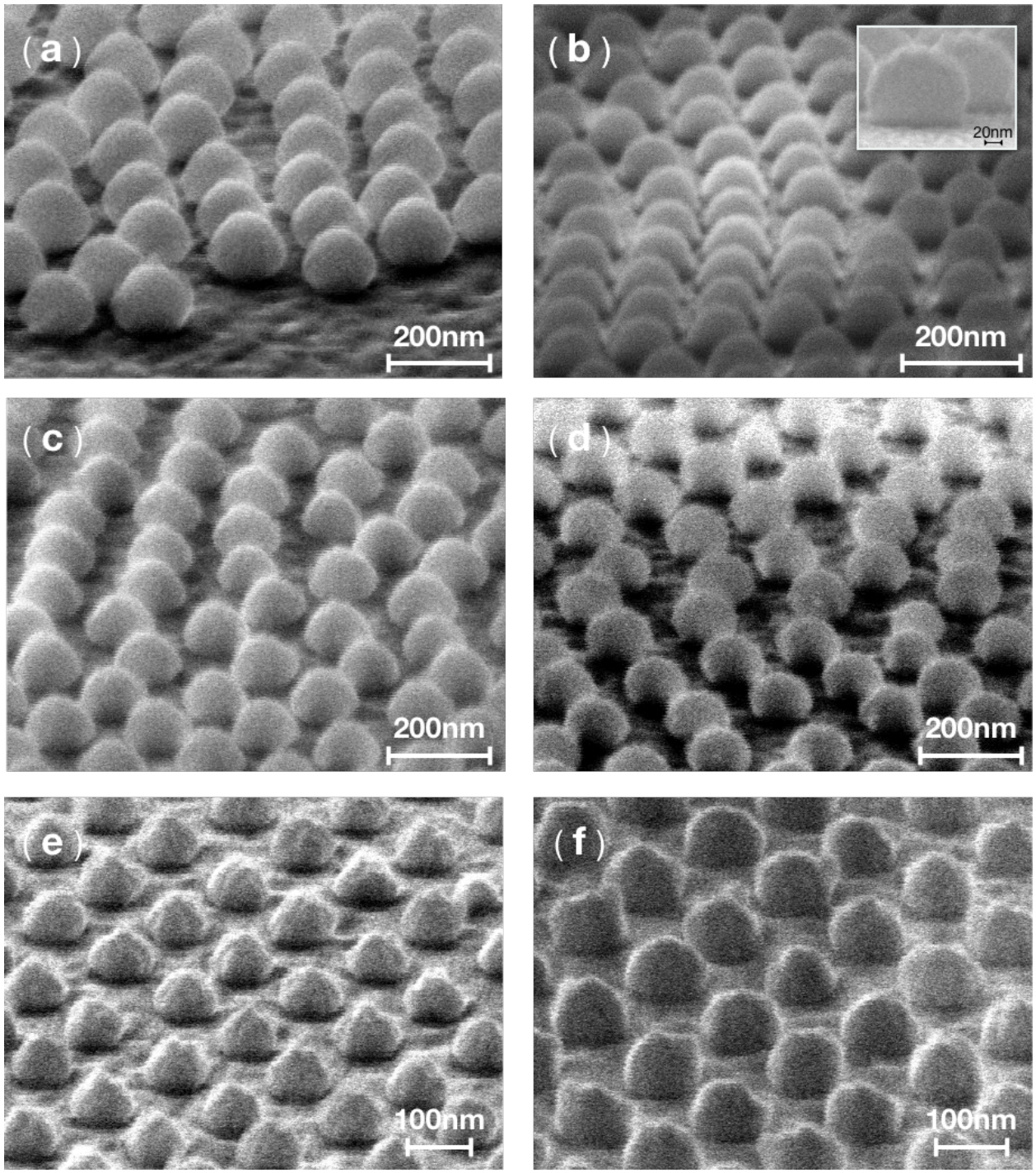

Figure 4.12 SEM images taken at a 70 degree tilted angle for PS spheres with different oxygen RIE treatment time: (a) PS spheres processed by oxygen plasma for 40 s; (b) PS spheres processed by oxygen plasma for 40 s and then 5mins annealing at 130 ℃, the inset is a magnified picture taken at 80 degree; (c) spheres processed by oxygen plasma for 60 s; (d) spheres processed by oxygen plasma for 60 s and then 5 min annealing at 130 ℃;

(e) spheres processed by oxygen plasma for 80 s; (f) spheres processed by oxygen plasma for 80 s and then 5 min annealing at 130 C°.

The tilted images clearly demonstrate that annealing at 130 ℃ for 5 minutes would sufficiently lead to the kind of deformation of spheres that we proposed in Fig 4.10. Comparing the spheres before annealing in Fig 4.12 (a), (c) and (e) with after annealing in (b), (d) and (f), noticeable change in spheres' shape including an increase of the area in contact with the underlying substrate, a decrease in the spheres' height and surface roughness were observed.

4.2 Substrate Preparation

Etch of the silicon dioxide by RIE is a difficult task; for MEAR applications it is especially true because ultra-fine structures with high aspect ratio are required. On the other hand, silicon dry etch is a well-studied field and fine structures with flexible etch profile and high aspect ratio can be fabricated. Therefore, for the purpose of this research, we present a novel and scalable fabrication technique for which flexible height and profile control can be achieved for MEAR structures.

As illustrated in Fig. 4.13, 1050 nm-thick poly-silicon with high uniformity was first deposited on the 4-inch transparent fused silica substrate by LPCVD technique for the fabrication of moth-eye biomimetic structures. Taking advantage of the well-developed silicon dry etch techniques, subwavelength moth-eye structures will be created on silicon before the final thermal oxidation process. During the LPCVD step, deposition took place on both sides of the fused silica glass. Since we are targeting to employ MEAR on one side of the glass, the backside poly-silicon was then entirely removed by an isotropic plasma etch in sulfur hexafluoride (SF_6); however, it does leave an option for double sided antireflective patterning. The thickness of poly-Si determines

the upper limit for the height of moth-eye structures. For structures of height shorter than 1 μm, the excessive silicon on the frontside was also removed before patterning. Finally, 30 nm of aluminum was deposited on the top by either e-beam evaporation or sputtering.

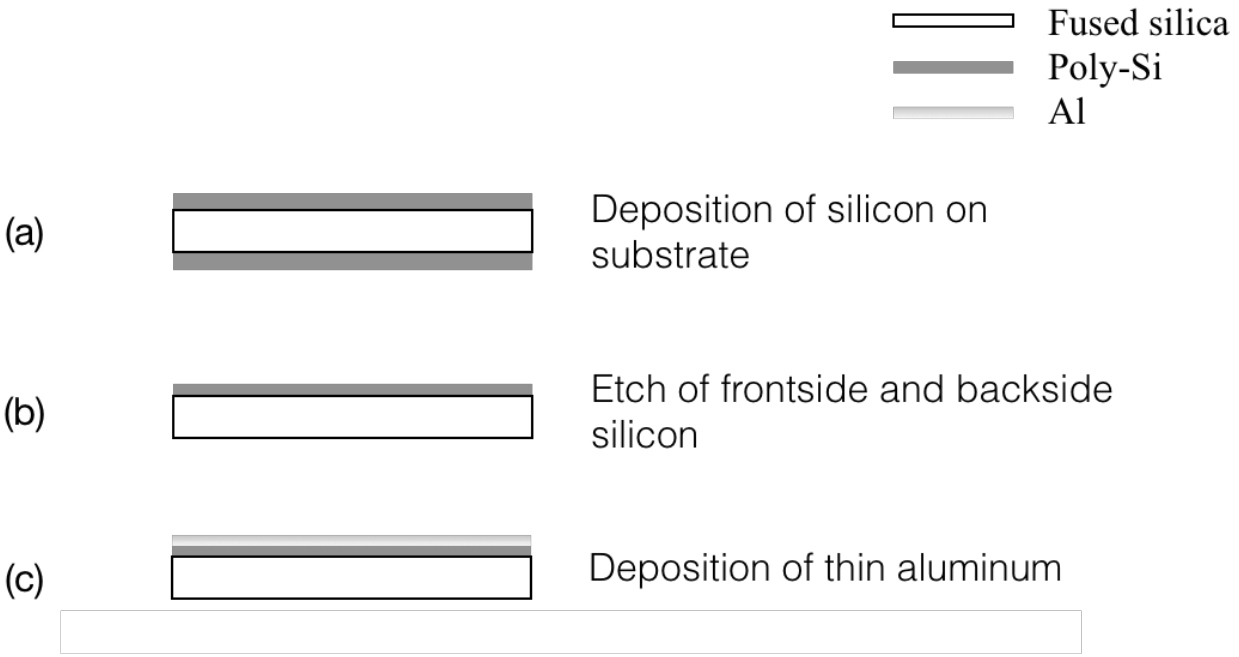

Figure 4.13 Schematic process of the substrate preparation: (a) deposition of poly-silicon on fused silica, (b) RIE of the frontside and backside silicon, (c) deposition of thin aluminum layer on top of the frontside silicon.

Although nanosphere lithography is a cost-effective and simple process for producing defect-free template with periodic arrangement, the primary drawback is that the colloids often feature a very low etching selectivity with respect to the substrate materials, such as silicon and silicon dioxide.

For polymeric nano-beads especially, they are good in terms of the flexibility of post modification, but as etch masks they are unable to produce structures with high aspect ratio mostly because of their poor mask-to-substrate selectivity. Therefore, a thin metal layer of aluminum is

used as second mask in our process, which offers great mask-to-substrate selectivity with respect to silicon. Original pattern was transferred from PS spheres to the metal layer first, patterned alumina was then used as mask for the polysilicon etching.

4-inch fused silica with poly-Si and aluminum on top was then cut into small pieces by dicing saw, and a plasma treatment was implemented to increase the surface wettability and adhesion before the Langmuir-Blodgett deposition.

4.3 Pattern Transfer by Reactive Ion Etching

Reactive ion etching plays an important role in creating the nanopillar arrays. As shown in Fig. 4.14, our entire fabrication process consists of six steps:

1. Preparation of substrate, including the deposition and removal of poly-Si, deposition of aluminum and plasma surface treatment.
2. Coating of the hcp colloid monolayer by a simplified Langmuir-Blodgett (LB) deposition.
3. Post-treatment of the colloid particles, including size reduction and annealing of PS nanospheres.
4. Reactive ion-etching of aluminum, pattern transferred from hncp nanosphere to aluminum.
5. Reactive ion-etching of silicon, pattern transferred from metal mask to silicon with a controlled tapered profile.
6. Residual polymeric spheres and aluminum removal and thermal oxidation of silicon.

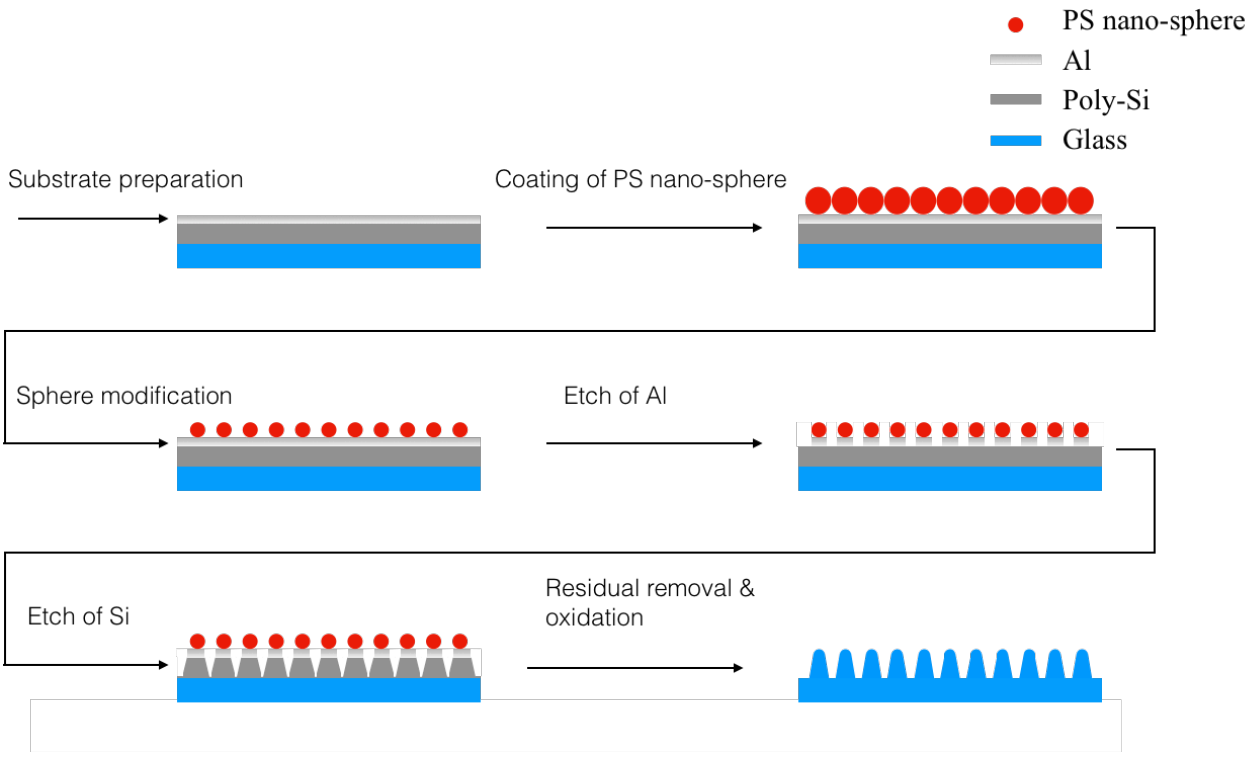

Figure 4.14 Process flow for the fabrication of cover glass with MEAR structures.

4.3.1 Reactive Ion Etching of Aluminum

Aluminum is typically dry etched in a BCl_3 - Cl_2 gas mixtures, yielding $AlCl_3$ as a volatile product which is pumped away[74]. The BCl_3 can fastly remove the aluminum as well as the commonly existing aluminum oxide, while Cl_2 is much more reactive than BCl_3 and the addition of Cl_2 boosts the etch rates[75].

In our process, since the aluminum layer was thin--only 30 nm thick, using BCl_3 alone would be sufficient to transfer the pattern from the PS template. Another reason for choosing thin metal layer is the low mask-to-substrate selectivity between PS and aluminum, close to 1:1 according to our measurement. It was found that the PS mask after proper annealing (cap-like shaped) could achieve a faithful pattern transfer on the thin aluminum by BCl_3 RIE, whereas PS mask before annealing (irregular shape) resulted in a noticeable dimension loss.

Using the plasma and thermal-modified PS as masks, aluminum was etched for 20 sec using an Oxford ICP-RIE system (ICP 380) with the recipe: BCl_3 50 sccm, RF power 300 W, ICP power 800 W, pressure 1 mTorr at 22℃. The measured etching rate was 110 nm/min. During the reactive ion etching, the area of aluminum covered by the modified cap-like PS spheres was protected while the rest directly exposed to the plasma was removed.

The aluminum etching result was confirmed by using atomic force microscope. As illustrated in Fig. 4.15, arrangement of the PS spheres was successfully transferred to the underlying aluminum.

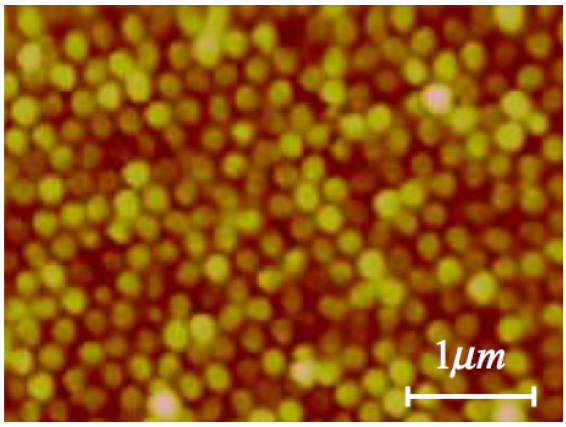

Figure 4.15 Atomic force microscope scan result of aluminum etch profile.

4.3.2 Reactive Ion Etching of Silicon

The reactive ion etching of silicon was performed right after the patterning of aluminum. Although the vertical etch profile with no dimension loss between mask and etched structures is favorable in most of the micro- and nano- fabrication process, for the application of moth-eye antireflection, pillars with tapered profile are actually preferred for the realization of GRIN region in which the effective refractive index is gradually increased[15, 76].

Developed by Robert Bosch GmbH[77], the Bosch process has become the most popular silicon deep reactive ion etching (DRIE) technique used in state-of-the-art DRIE equipment. The Bosch process is implemented in a pulsed-mode where each cycle commonly comprises two separate steps. As depicted in Fig. 4.16: a short-time etching with SF_6 plasma is performed at the beginning where both the mask and substrate are etched in a relatively isotropic manner; in the

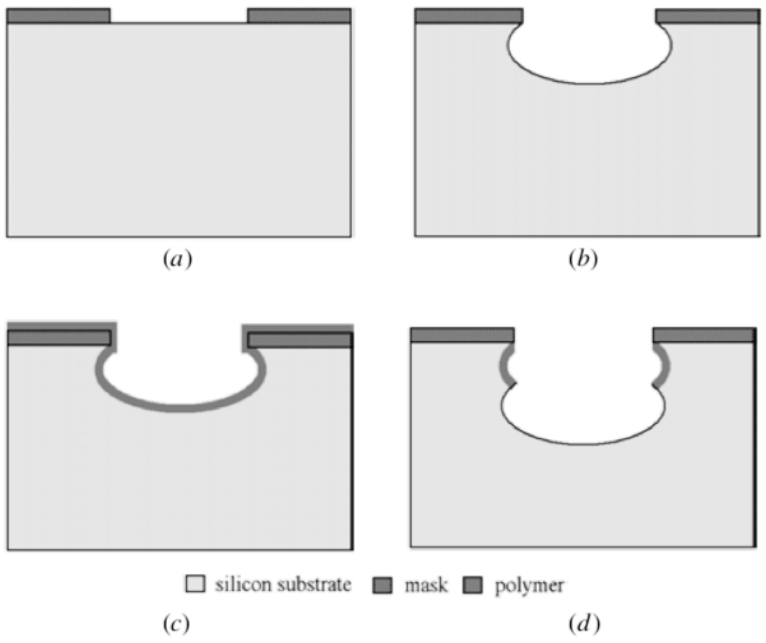

Figure 4.16 A schematic of the Bosch process: (a) pre-patterned silicon substrate; (b) etching step; (c) polymerization step; (d) next etching step [76].

following step, inhibitor layer of fluro-carbon polymer is deposited on the exposed silicon surface as well as on the mask by C_4F_8 gas; then it alternates to the new etch step where polymer at the bottom is quickly removed by ion bombardment and the uncovered silicon is hence etched by the etchant. Although a single etching step is quite isotropic, the overall effect of anisotropy is achieved by the combination of etching and passivation. As a result, the depth of structures increases with the number of cycles without much lateral etching. For majority of its applications,

the Bosch process is used for etching with a vertical profile where structures retain the critical dimension of the masks, but tapered profile is indeed achievable, for instance, by modifying the SF_6 etching step[76].

Although standard Bosch process is easy to handle and robust with respect to the pattern layout, there is one downside that the pulsed-mode will inherently introduce the scalloping effect to the structures[78]. However, this sidewall scallops can be prohibited in a mixed-mode RIE process in which gases are simultaneously introduced to the chamber without switching steps. A comparison between the etch profiles of trenches by two RIE mode is shown in Fig. 4.18, which clearly illustrates the differences.

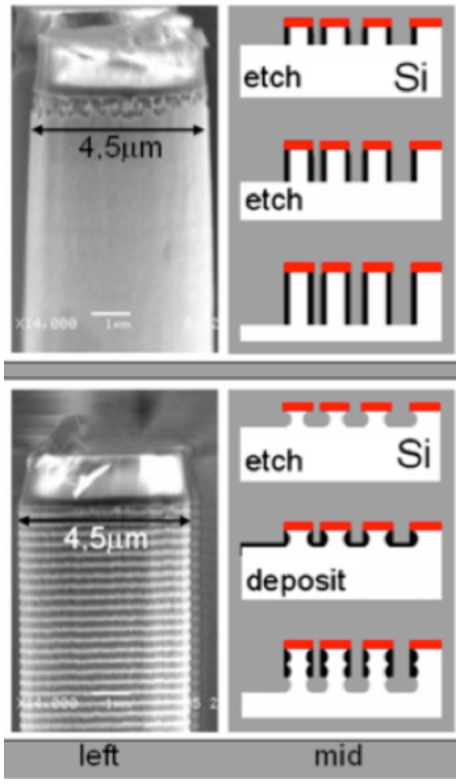

Figure 4.17 Cross-sectional views of Si trenches etched by mixed-mode versus pulsed-mode [77].

Another advantage of the mixed-mode Si RIE for our purpose is that the etch profile is proven much more controllable and tunable than the pulsed Bosch process. It is reported that tapered angle as large as 39° can be achieved with a non-switching C_4F_8/SF_6 recipe[76]. This finding is of great importance for our process since MEAR pillars with tapered profile are preferred for the realization of GRIN region[27]. By introducing both kinds of gases together, while neutral fluorine radicals released by SF_6 still contribute the most to the removal of Si[79], the presence of C_4F_8 provides steady-state inhibitor film that are against the Si etching[80]. As a result of the two competing sub-processes, one can obtain a tapered profile by increasing passivation and decreasing etching.

There are also challenges when etching with tapered profile. The first is the less efficient Si etching, which means the etch rate is reduced due to the enhanced inhibitor formation. The second is the happening of undercut due to reduced etch anisotropy.

For our fabrication process, a reduced Si etch rate is generally acceptable because the thickness of Si layer is less than 1 μm. The increased undercut (over-etched under the mask) will cause dimension loss between the etched pillar and the aluminum mask, in which the final pillar diameter at the top is smaller than the mask. This places a new demand on the diameter of aluminum: if the aluminum mask is not sufficiently large, as the non-switching C_4F_8/SF_6 etching proceeds, the etch will become totally maskless once the top of silicon pillars cannot uphold the aluminum mask above. Since the diameter of aluminum mask depends on the dimension of PS nanosphere, in order to ensure that the etched pillars are well defined, it is therefore critical that the diameter of spheres must be above a minimum value after the size reduction.

To obtain the tapered profile, RIE of Si by using the recipe reported in [74] in mixed-mode was carried out on the substrate with patterned aluminum using the Oxford ICP-RIE system (ICP 380). In the experiments, while the ratio of C_4F_8/SF_6 was increased from 40/20 to 52/8, the other

parameters were fixed as illustrated in Table 4-1. Selective etch results by different gas ratios are shown in Fig 4.18.

Table 4-1 Recipe for mixed-mode RIE of silicon that gives tapered etched profile

RF power (W)	ICP power (W)	Pressure (mTorr)	Temperature (°C)	Total gas flow (sccm)	C_4F_8/SF_6
30	1200	10	15	60	40/20~52/8

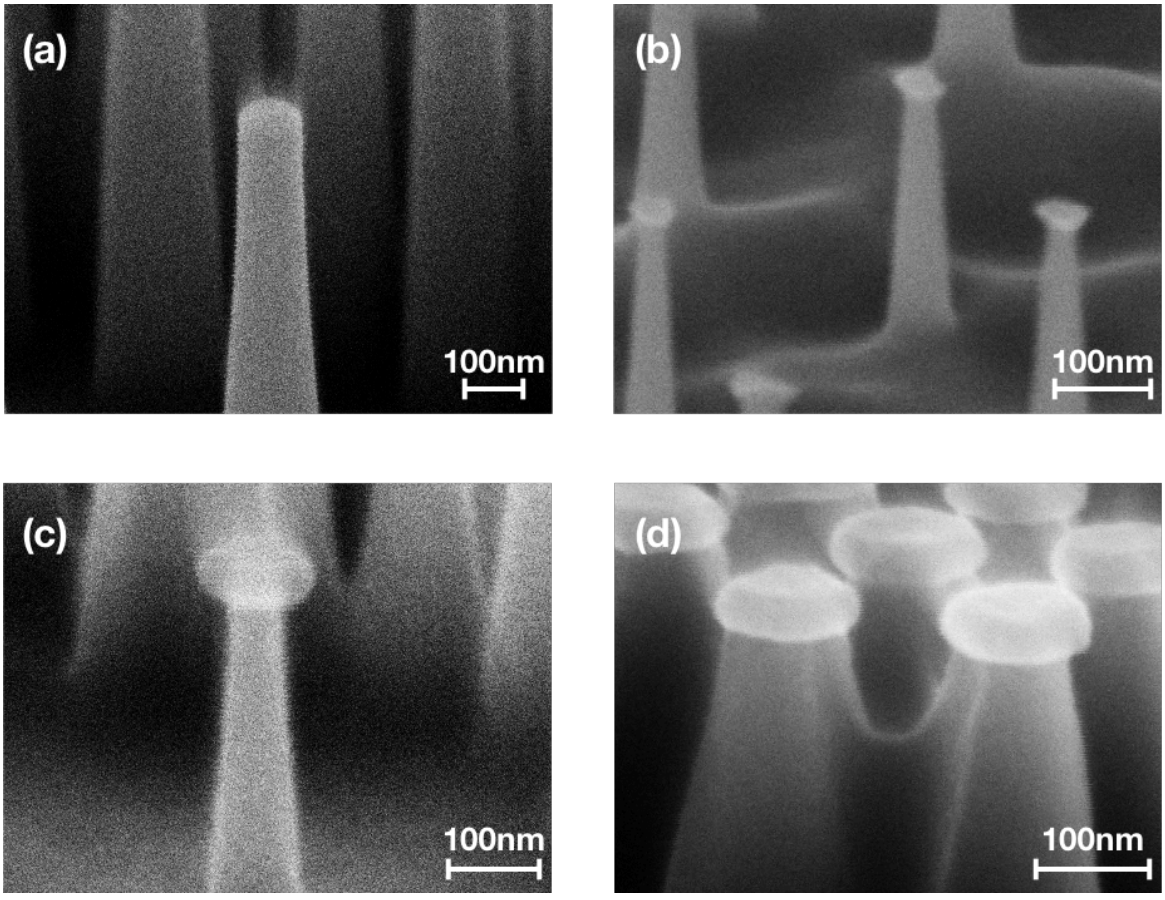

Figure 4.18 70° tilted SEM images of silicon structures etched with different C_4F_8/SF_6 ratios. The ratios and measured sidewall tapered angles are: (a) 40/20, 2°; (b) 44/16, 4.1°; (c) 46/14,

6.9°; (d) 52/8, 16.7°. The aluminum masks were not removed and can be seen in the images.

The results confirmed that the sidewall taper angle increases with the C_4F_8/SF_6 ratio at the cost of significantly reduced vertical etch rate. The calculated etch rates from pillar height measurements decreased from 400 nm/min at gas ratio 40/20 to less than 70 nm/min at 52/8. We also noticed that by increasing the gas ratio, the undercut profile of silicon was enlarged because of the etch isotropy.

Fig. 4.19 gives an example that the shrunk pillar top cannot uphold the metal mask, resulting in the occurrence of tilted masks or missing masks. In consideration to these effects, C_4F_8/SF_6 ratio of 42/18 was chosen in all our experiments for its less lateral etching under aluminum masks and moderate etch rate around 140 nm/min and taper angle 2.8°.

It was found that for the fabrication process of MEAR structures we developed, PS sphere with a diameter of 130 nm (with 40 s oxygen plasma size reduction) are sufficient to enable the mixed-mode silicon RIE to etch a depth up to 1.4 μm.

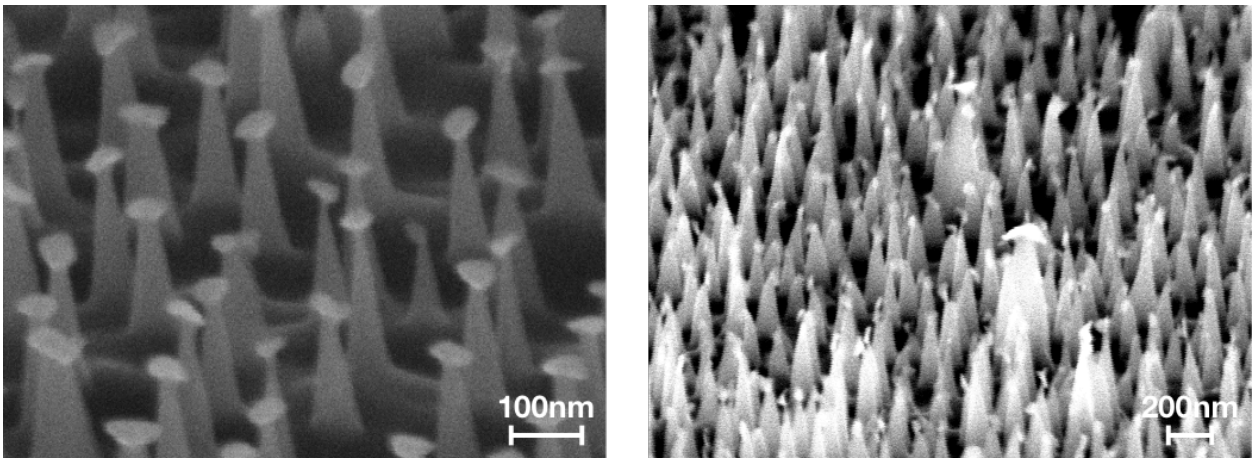

Figure 4.19 Examples of the influences of undercut on the aluminum mask.

Finally, for the fabrication of moth-eye structure with tapered profile, substrates with patterned aluminum mask were processed using the non-switching silicon etching recipe shown in Table 2.1, with a fixed C_4F_8/SF_6 ratio to be 42/18. Patterns on the aluminum masks were created by polystyrene nanospheres template which was shrank in oxygen plasma for 40 sec and annealed at 130 ℃ for 5 min. The quality of silicon etching was evaluated by taking SEM images at 70° tilted angle, as shown in Fig. 4.20 and 4.21. Fig. 4.20 displays the arrangement of an evenly spaced pillar array; the center to center distance between pillars depends on the diameter of self-assembly spheres, which was 200 nm. The structure produced though our process is free of large defect, and features uniform coverage over a large substrate area.

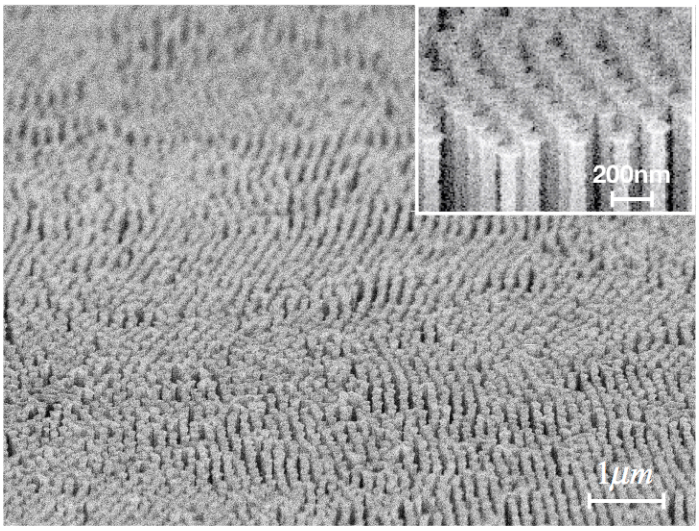

Figure 4.20 Tilted SEM picture of the top of moth-eye array, the inset is a zoom-in image at the array boundary.

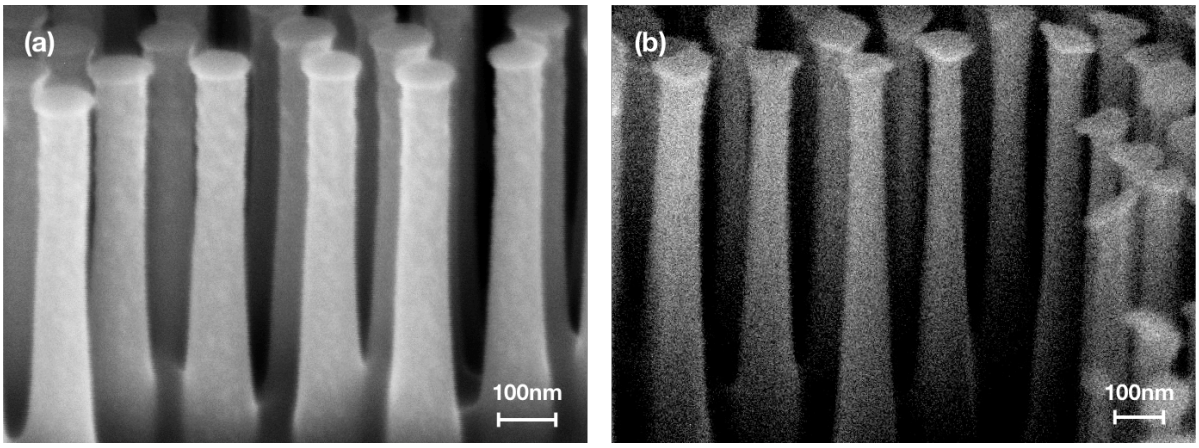

Figure 4.21 70° tilted SEM images of silicon moth-eye pillars etched with a fixed C_4F_8/SF_6 ratio of 42/18. (a) pillars with a height of 600 nm; (b) pillars with a height of 1000 nm.

By using the method presented above, it is possible to achieve well-defined hexagonally spaced subwavelength features with tunable sidewall profile control. From Fig. 4.21, pillars with 600 nm and 1 μm height all feature smooth and tapered sidewall profiles, with the undercut at the aluminum mask under control.

4.3.3 Thermal Oxidation

As discussed at the beginning of Chapter 4.3, thermal oxidation is the last step in our proposed process in pursuit of MEAR coverglass. In IC manufacturing the thermal oxidation is a broadly favored technique for the conversion of silicon to silicon dioxide, which can be carried out in either dry or wet ambient. The overall chemical reaction is:

$$\text{Dry oxidation:} \quad \mathrm{Si} + \mathrm{O_2} \rightarrow \mathrm{SiO_2} \tag{4.1}$$

$$\text{Wet oxidation:} \quad \mathrm{Si} + 2\mathrm{H_2O} \rightarrow \mathrm{SiO_2} + 2\mathrm{H_2} \tag{4.2}$$

The oxidation process is usually lengthy and therefore quite costly when involving the use of dedicated tube oxidation furnace. For the ease of operation as well as a low cost, dry oxidation of fused silica glass with patterned poly-silicon structures was performed at atmospheric environment

in a generic box furnace (shown in Fig. 4.22) rather than a dedicated tube. The reason is that prior study on the oxidation sharpening of silicon tips for atomic force microscope[81] has proven that, the oxide grown by this muffle furnace at atmospheric environment is of high purity, with only Si and O found in the film diagnosed by the energy-dispersive x-ray spectroscopy.

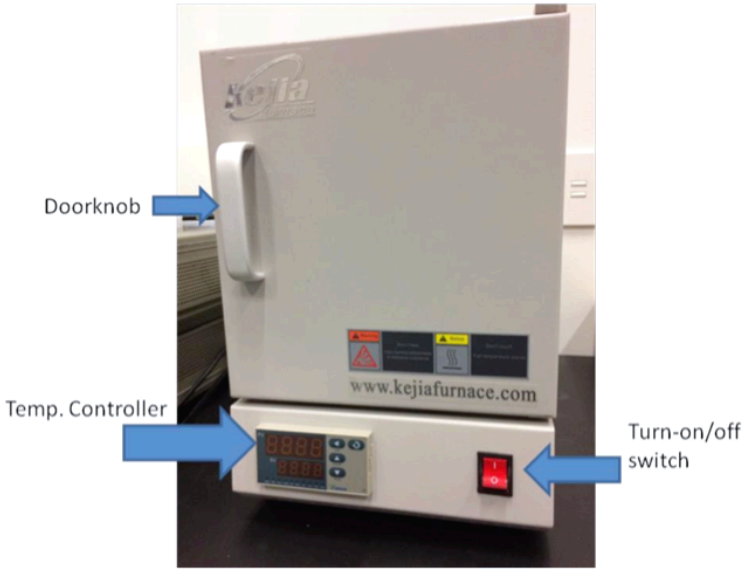

Figure 4.22 Picture of the hot furnace used for dry oxidation of silicon. By using resistive heating, a maximum temperature of 1200 C° can be reached with accurate heat up rate control within 0-15 C°/min.

For the oxidation of samples patterned with MEAR structures, the influence of temperature has to be considered. Although the high temperature leads to an increase in the oxide growth rate[81], it will also result in a decrease in the viscosity of oxide. At certain temperature the low viscosity will cause partial viscous flow of oxide that triggers the deformation of structures. It was reported the break point occurs at 1070 ℃, above which the stress because of structure curvature and lattice mismatch will be fully released[82]. A low temperature, however, is also not suitable in our case. This is because of the dependence of oxide density on the oxidation temperature; low

temperature oxide of poly-silicon features higher refractive index than that of high temperature oxide. For moth-eye structures, material with low refractive index is still preferred.

Oxidation temperature at 950 ℃ was selected as the process condition after consideration on the influences of oxidation temperature discussed above. The thickness of oxide grown by poly-silicon with respect to the total oxidation time was measured and shown in Fig. 4.23, with result of single-crystal silicon for comparison. As seen, the oxidation rate was faster in the first few hours than at longer time. This is because that for the initial growth the rate is mostly limited by the reaction rate, hence the thickness is almost proportional to the time; as the thickness of oxide increases, oxidizing species have to diffuse through the existing oxide before reaction with the silicon, the rate becomes diffusion limited, the thickness therefore increases with the square root of time.

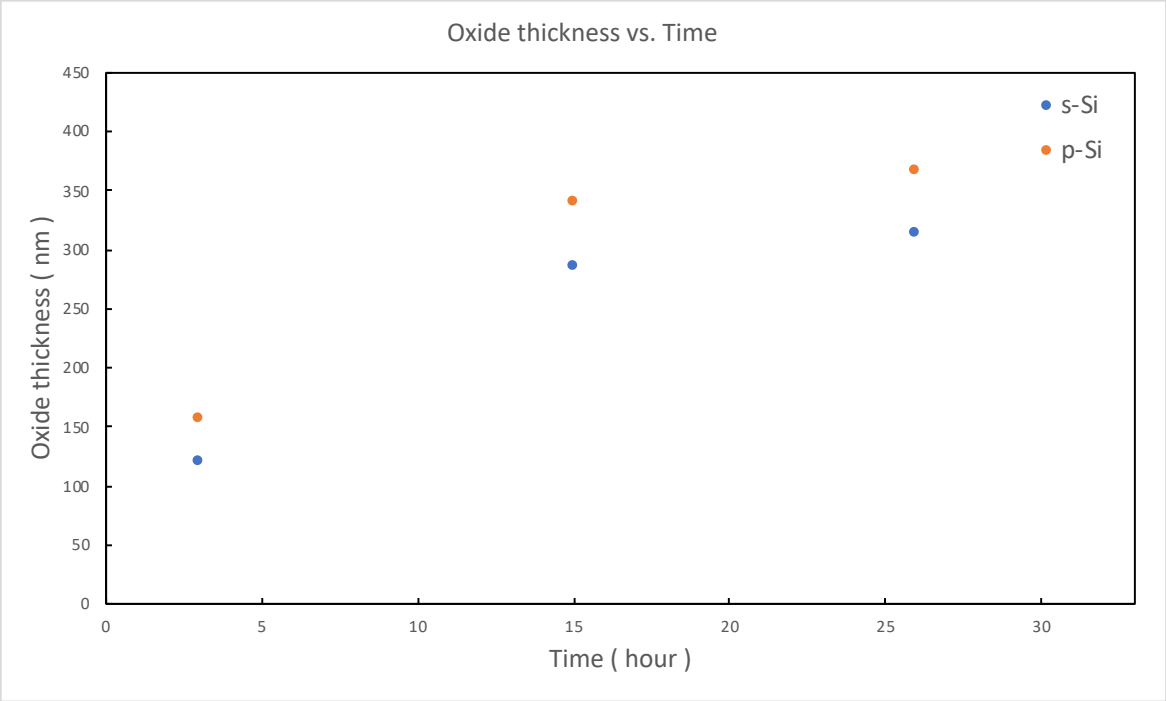

Figure 4.23 Measured oxide thickness with respect to the time at 950 C°.

For the fused silica samples with patterned silicon moth-eye structures, two additional steps were performed before the dry oxidation. The first is the oxygen plasma cleaning using the recipe in Table 4-2, which aims to remove the fluorinated-carbon polymer residuals. The second is the removal of remaining aluminum masks by wet etching in diluted hydrofluoric acid (1:50).

Table 4-2 Recipe for oxygen plasma cleaning

RF power (W)	ICP power (W)	Pressure (mTorr)	Temperature (°C)	O_2 gas flow (sccm)	Time (min)
20	500	20	22	50	5

The progress of oxidation was checked with the glass substrate patterned with 800 nm tall silicon pillar arrays after a 3-hour oxidation. By dipping samples in 1:10 diluted HF for 3 mins, thermally grown oxide was removed whereas un-oxidized silicon would remain. The tilted SEM picture (Fig. 4.24) was taken after the deposition of around 20 nm aluminum conductive layer by sputtering for reducing the charging effect.

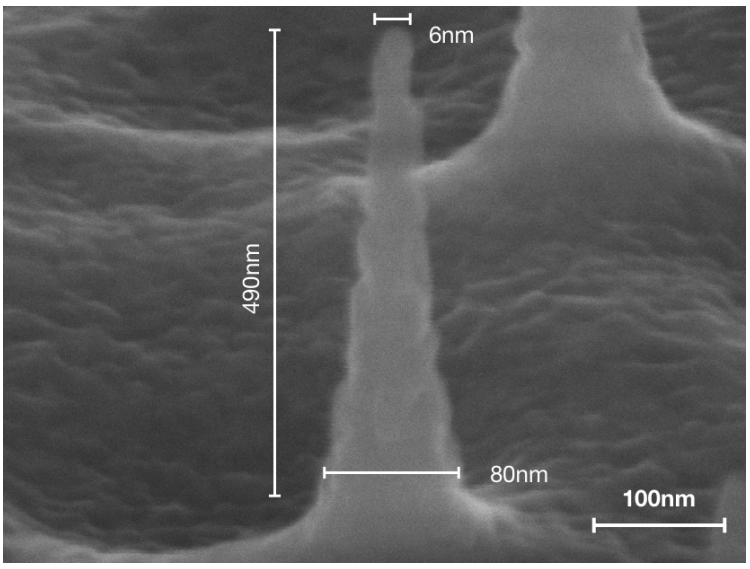

Figure 4.24 70° tilted SEM images of the examined sample after oxide removal.

Un-oxidized silicon cores were spotted after the removal of thermally grown oxide. Pillars exhibited a 300-nm decrease in the height, whereas the width of pillar at the base barely changed. The observed oxidation rate was much larger at the upper part of individual pillar than that close to the bottom. It can be concluded that oxidation for 3 hours is not even close to the finish. It was beyond expectation that a total of around 35 hours were needed for the entire oxidation process; this was possibly because of the significant drop of oxidation rate once the newly grown oxide gets thicker. Fig. 4.25 is a picture of a piece of fused silica glass with poly-silicon (800 nm thick) on top and a piece of fused silica applied with the 800-nm-tall MEAR structures by our process (the dimension of samples is $3 \times 3.5\ cm^2$).

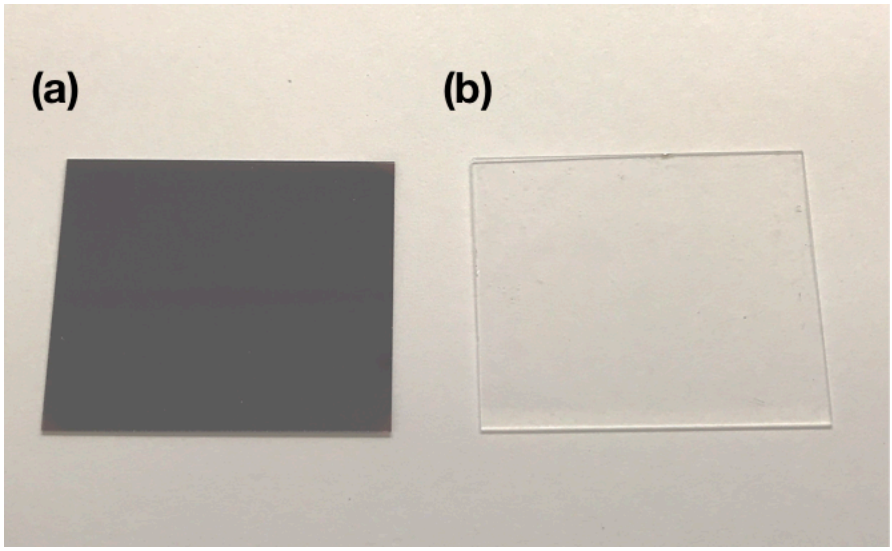

Figure 4.25 Picture of (a) fused silica substrate with 800 nm of poly silicon, (b) fused silica substrate patterned with 800-nm-tall moth-eye structures after the oxidation process.

The profile of oxidized subwavelength structures was examined again after the dry thermal oxidation, and the whole sample became transparent as expected. Metal conductive layer was also deposited to reduce the charging effect during SEM. Fig. 4.26 shows the profiles of oxidized moth-eye pillars at the boundary of the array.

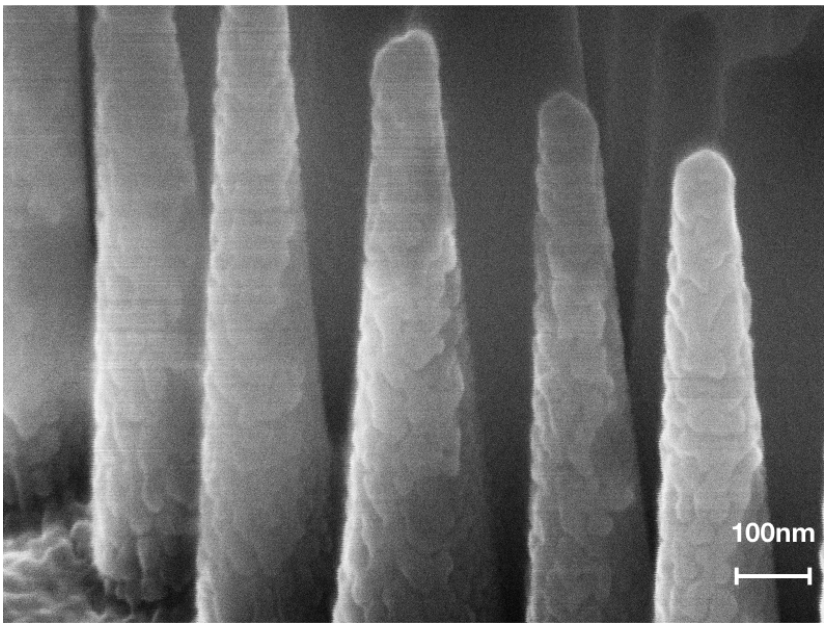

Figure 4.26 Tilted SEM picture of MEAR structure after the oxidation.

The oxide moth-eye pillars feature the same arrangement as the silicon pillars, with a slightly tapered sidewall profile which is favored for the formation of a gradient refractive index region. There is no obvious change in the height of structures, only around 10~20 nm based on the SEM images. However, the pillar exhibits a lateral expansion in volume so that the bottom part of each pillar gets connected to another. As a result, oxidizing species have to diffuse through a thicker oxide before reacting with the inner silicon, which is one possible reason for the prolonged oxidation process.

Chapter 5 Reflectance Measurement of Anti-Reflective Glass

Following the fabrication method proposed in the previous chapter, fused silica glass with one-side patterned moth-eye structures featuring heights of 600 nm, 800 nm and 1000 nm were produced. Optical measurement of reflectance was then carried out to evaluate the anti-reflective performance of the coverglasses.

5.1 Reflectance at Normal Incidence

The total reflection (specular & diffuse) of samples was measured by a dual-beam, high resolution spectrophotometer with an integrating sphere (Cary 5000 UV-Vis-NIR, Varian Inc.) after instrument calibration. The measurement setup is depicted in Fig. 5.1 (a)[83]. Samples were tilted by a small angle of 4° so that the specularly reflected light hits the integrating sphere and therefore collected.

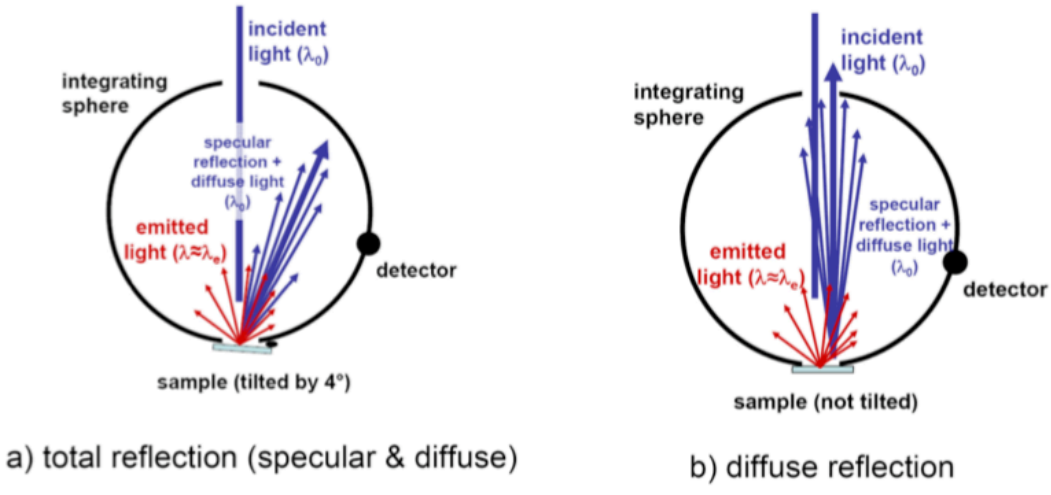

Figure 5.1 Common setups for reflection measurements with an integrating sphere [82].

In our experiment, measurement results comprise reflectance caused by both front patterned surface and the back unpatterned surface. Since the key here is to evaluate the influence of the structures in the front, the measurement is therefore insensitive to backside reflection. By comparing the total reflectance of samples with that of bare glass, we can then have the relative decrease which represents the improvement. Fig. 5.2 illustrates the reflectance measurement results of glass samples with different pillar heights in the spectral range from 250 nm to 1200 nm.

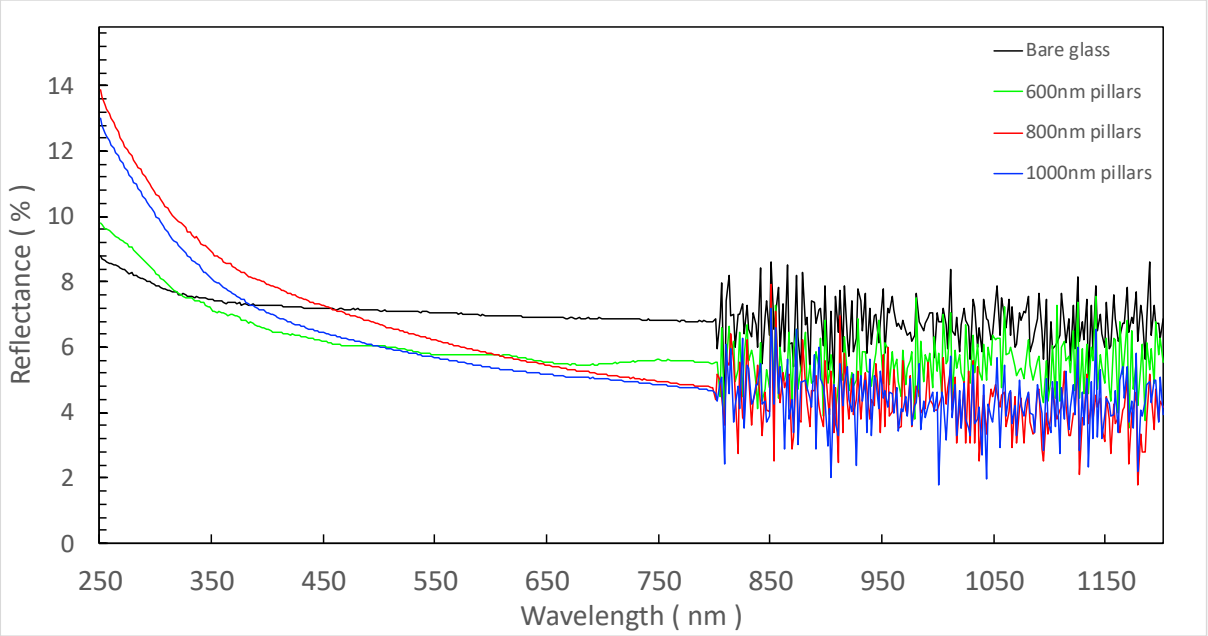

Figure 5.2 Measured reflectance with respect to the wavelength.

The anti-reflective performance of MEAR treated glass is confirmed from the above measurement. With tapered geometrical profiles of the densely placed nanopillars that can offer a smooth transition for the surrounding air to the substrates, an enhancement of up to 2% in the anti-reflective performance is achieved in the wavelength range from 450 nm to 1200 nm. Substrates equipped with high pillars give lower reflectance in the long wavelength, whereas short pillars offer better spectral coverage. It was noticed that an increase of reflectance as compared to un-patterned glass occurs at short wavelength range. The possible reason is the collected diffuse

reflection by the integrating sphere. As was discussed in Chapter 2, for the structures to be considered as having effective gradient refractive index, the pitch has to be much smaller than the wavelength of light, which is the subwavelength regime or the long wavelength limit. For the spectral range smaller than 450 nm, since the period of patterned pillars is 200 nm in our study, it no longer satisfies the requirement, and the scattering caused by bumpy surface will arise. The mixture of specular and diffuse reflection collected by the integrating sphere results in the jump of measurement at short wavelength.

5.2 Reflectance at High Oblique Angles

The omni-directional anti-reflective characteristics of fabricated MEAR coverglass was examined by a spectroscopic ellipsometer (M-2000, J. A. Woollam). Reflectance was acquired at incident angles from 55° to 75° which is the upper limit of the equipment with 5° increment. By measuring the amplitude of ellipse, the ellipsometer directly gives information about the light intensity. After baseline correction, measurements were performed for samples with different heights of pillars and bare fused silica glass, and some of the results are shown in Fig. 5.3 and 5.4.

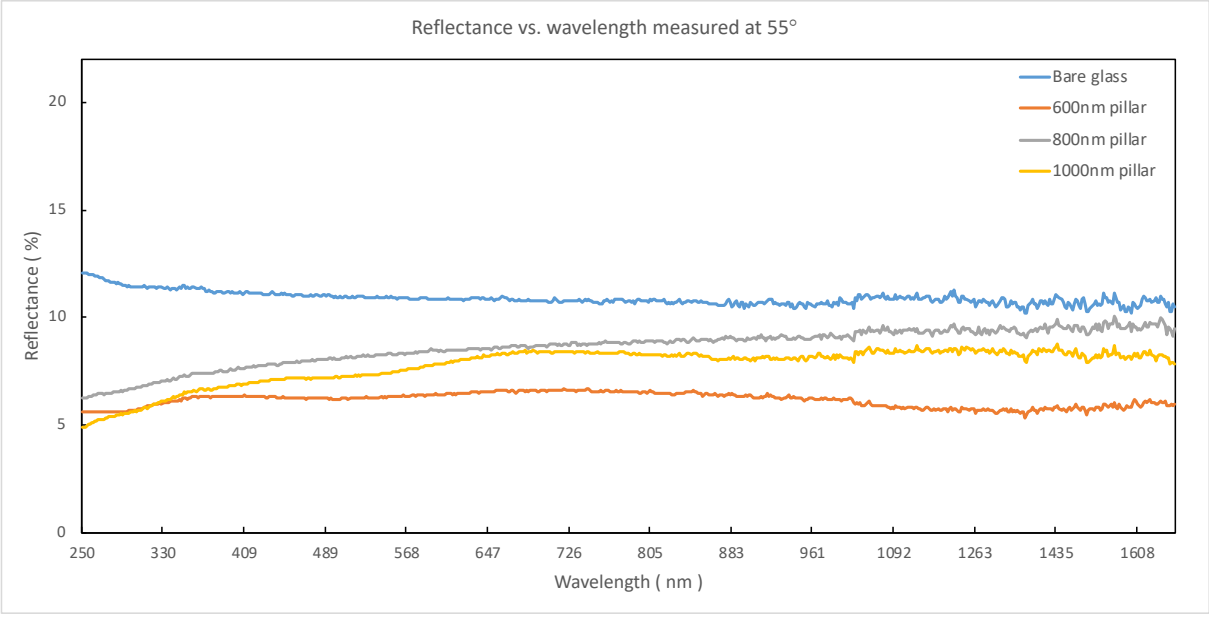

Figure 5.3 Ellipsometric reflectance curves at incidence angle of 55°.

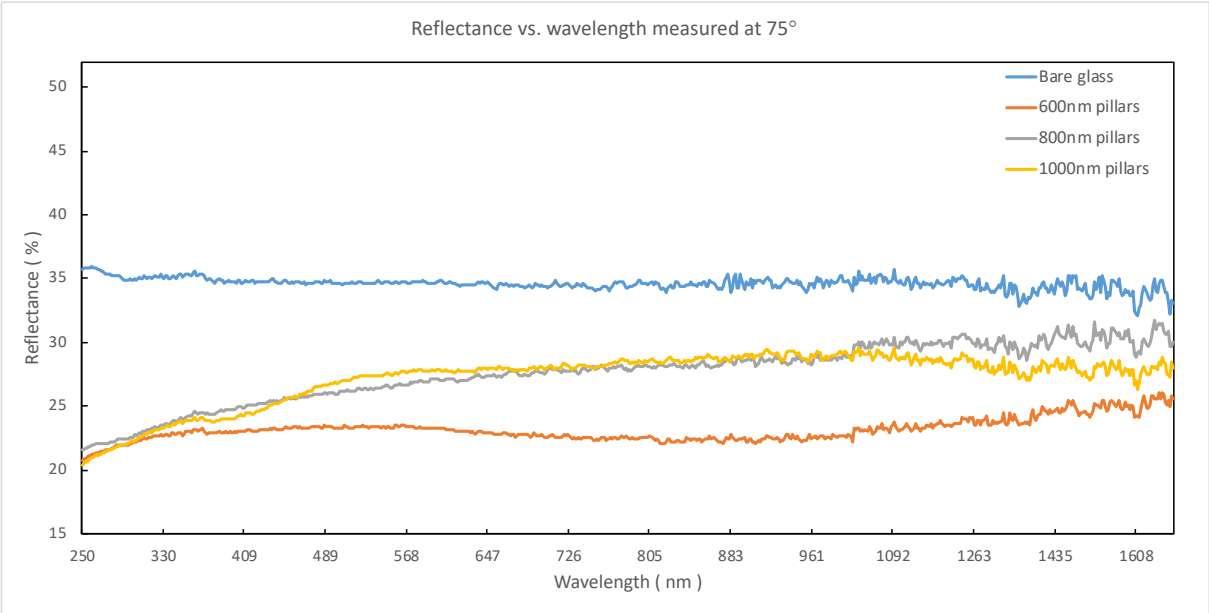

Figure 5.4 Ellipsometric reflectance curves at incidence angle of 75°.

As expected, the broadband antireflection properties of MEAR treated surface exist even at oblique angles. At an incident angle of 55°, the reflectance of bare glass barely changes, with a narrow dispersion from 12% to 10%. In comparison, samples textured with nanopillars all feature lower reflectance throughout the whole range of wavelength. While pillars of 800 and 1000 nm heights deliver close antireflective performance, the 600 nm textured glass surpasses the others, with a superior reflectance lower than 6% within the wavelength of interest.

Increase of reflectance is observed on all samples as the incident angle changes from 55° to 75°. All samples with nanopillars perform better than bare glass in reducing reflection, but fused silica with 600 nm pillar on top delivers the best anti-reflective performance, with an averaged specular reflection more than 10% smaller than that of bare glass. Due to the very special application of the MEAR treated glass in which CubeSats often experience high incident angle

and has a short dwell time during mission, an on-orbit demonstration is on the way to further validate the influence of increased antireflective performance on the CubeSats' working status.

Chapter 6 Conclusion

The development of nanosatellites significantly lowers the barrier of entry into space. The reported growing annual number of planned launches represents the enthusiasm in conducting space missions with nanosats, especially one particular type of it, which is the CubeSats. The modular technique of CubeSats allows the use of more commercial off-the-shelf (COTS) rather than customized components for their structure and electronics, which fundamentally reduces the turnaround time as well as the expense. Universities and private companies account for a large portion of the CubeSats projects and they actively build the CubeSats for scientific and commercial objectives. A successful mission relies on the cooperation of all satellite subsystems, particularly the power generation subsystem. Applying moth-eye antireflection technique to the already existing coverglass of solar cells on CubeSats paves the way to improve the overall power generation ability without placing demand on the weight and volume.

In this study, we proposed a novel, scalable fabrication process of applying MEAR structures on the fused silica glass for space applications. With the help of modern nanofabrication techniques such as evaporation, sputtering, low pressure chemical vapor deposition and reactive ion etching, a non-lithographic double mask patterning fabrication process was carried out. Colloidal lithography was utilized for the creation of initial arrangement of structure. The modification of polystyrene nanospheres by annealing was first introduced for the production of biomimetic structure, and the deformation of sphere during thermal treatment was experimentally investigated. Mixed-mode reactive ion etching that can deliver tunable etch profiles was used in creating high aspect ratio moth-eye pillars. Confirmed with scanning electron microscopy imaging, hexagonally arranged high aspect ratio pillars with tapered sidewall profile was successfully fabricated.

Improvements are to be made to investigate the influence of side wall taper angle of the structure on the antireflective performance, the challenge is that by increasing the taper angle during silicon etching, huge undercut occurs on the pillar top and destroy the structure.

Overall, a scalable and highly versatile fabrication method was proposed, which enables the patterning of nanopillars of different heights, periods as well as profiles on the glass substrate. At normal incidence, we achieved a 2-4% decrease in the reflectance. This is below our goal but still a meaningful improvement because based on the work in [84] that even a 2% drop in reflectance brought 1.7% increase in the power generation. Moreover, the performance was demonstrated better at glancing angles. The high angle measurements showed an average of 5% to more than 10% lower than bare glass in the reflectance from 300nm to 1200nm wavelength. With the demonstration of broadband and omni-directional anti-reflective properties of the fabricated MEAR coverglass, we believe that the MEAR treated glass is highly beneficial for enhancing the power generation ability of solar cell on CubeSats, which usually experience high incident angles towards sunlight.

Reference

[1] United Nations Office for Outer Space Affairs. Outer Space Objects Index [Online]. Available: http://www.unoosa.org/oosa/osoindex/index.jspx?lf_id=

[2] SpaceWorks Enterprises, "Nano Microsatellite Market Assessment," ed. Atlanta, Georgia, 2014.

[3] M. Swartwout, "The first one hundred CubeSats: A statistical look," *Journal of Small Satellites,* vol. 2, pp. 213-233, 2013.

[4] SpaceWorks Enterprises, "Nano/Microsatellite Market Forecast," ed. Atlanta, Georgia, 2017.

[5] J. Bouwmeester and J. Guo, "Survey of worldwide pico- and nanosatellite missions, distributions and subsystem technology," *Acta Astronautica,* vol. 67, no. 7-8, pp. 854-862, 2010.

[6] D.-S. Kim, M.-S. Park, and J.-H. Jang, "Fabrication of cone-shaped subwavelength structures by utilizing a confined convective self-assembly technique and inductively coupled-plasma reactive-ion etching," *Journal of Vacuum Science & Technology B,* vol. 29, no. 2, p. 020602, 2011.

[7] J. W. Leem, Y. M. Song, Y. T. Lee, J. S. Yu, J. Ihm, and H. Cheong, "Effect of AZO deposition on antireflective property of Si subwavelength grating structures," pp. 183-184, 2011.

[8] D.-S. Kim, S.-H. Eo, and J.-H. Jang, "Direct integration of subwavelength structure on a GaAs solar cell by using colloidal lithography and dry etching process," *Journal of Vacuum Science & Technology B: Microelectronics and Nanometer Structures,* vol. 31, no. 3, p. 031202, 2013.

[9] C.-H. Sun, W.-L. Min, N. C. Linn, P. Jiang, and B. Jiang, "Templated fabrication of large area subwavelength antireflection gratings on silicon," *Applied Physics Letters,* vol. 91, no. 23, p. 231105, 2007.

[10] K. Watanabe, J. Yamamoto, and R. Tsuchiya, "Broadband-antireflective hybrid nanopillar array for photovoltaic application," *Journal of Applied Physics,* vol. 118, no. 8, p. 085102, 2015.

[11] B. Jin and J. He, "Self-Templated Fabrication of Robust Moth-Eye-Like Nanostructures with Broadband and Quasi-Omnidirectional Antireflection Properties," *ACS Photonics,* vol. 4, no. 1, pp. 188-196, 2017.

[12] H. Podmore, "Subwavelength antireflection for space applications," Master's, York University, 2015.

[13] E. C. Garnett and P. Yang, "Silicon Nanowire Radial p−n Junction Solar Cells," *Journal of the American Chemical Society,* vol. 130, no. 29, pp. 9224-9225, 2008/07/01.

[14] S. Ji, K. Song, T. B. Nguyen, N. Kim, and H. Lim, "Optimal moth eye nanostructure array on transparent glass towards broadband antireflection," *ACS Appl Mater Interfaces,* vol. 5, no. 21, pp. 10731-7, Nov 13 2013.

[15] Y. M. Song, H. J. Choi, J. S. Yu, and Y. T. Lee, "Design of highly transparent glasses with broadband antireflective subwavelength structures," *Optics Express,* vol. 18, no. 12, pp. 13063-13071, 2010/06/07.

[16] H. K. Raut, S. S. Dinachali, K. K. Ansah-Antwi, V. A. Ganesh, and S. Ramakrishna, "Fabrication of highly uniform and porous MgF2 anti-reflective coatings by polymer-based sol-gel processing on large-area glass substrates," *Nanotechnology,* vol. 24, no. 50, p. 505201, Dec 20 2013.

[17] G. Tan *et al.*, "Broadband antireflection film with moth-eye-like structure for flexible display applications," *Optica,* vol. 4, no. 7, 2017.

[18] L. Rayleigh, "On the Propagation of Waves through a Stratified Medium, with Special Reference to the Question of Reflection," *Proceedings of the Royal Society of London. Series A,* 10.1098/rspa.1912.0014 vol. 86, no. 586, p. 207, 1912.

[19] Wikipedia. *Anti-reflective coating*. Available: https://en.wikipedia.org/wiki/Anti-reflective_coating

[20] P. Vukusic and J. R. Sambles, "Photonic structures in biology," *Nature,* 10.1038/nature01941 vol. 424, no. 6950, pp. 852-855, 2003/08/14.

[21] S. J. Wilson and M. C. Hutley, "The Optical Properties of 'Moth Eye' Antireflection Surfaces," *Optica Acta: International Journal of Optics,* vol. 29, no. 7, pp. 993-1009, 1982/07/01.

[22] P. I. Stavroulakis, S. A. Boden, T. Johnson, and D. M. Bagnall, "Suppression of backscattered diffraction from sub-wavelength 'moth-eye' arrays," *Optics Express,* vol. 21, no. 1, pp. 1-11, 2013/01/14.

[23] T. C. Choy, *Effective Medium Theory: Principles and Applications*, illustrated, reprint ed. Clarendon Press, 1999, p. 182.

[24] S. A. Boden and D. M. Bagnall, "Bio-Mimetic Subwavelength Surfaces for Near-Zero Reflection Sunrise to Sunset," in *2006 IEEE 4th World Conference on Photovoltaic Energy Conference*, 2006, vol. 2, pp. 1358-1361.

[25] K. Han and C.-H. Chang, "Numerical Modeling of Sub-Wavelength Anti-Reflective Structures for Solar Module Applications," *Nanomaterials,* vol. 4, no. 1, pp. 87-128, 2014.

[26] D. G. Stavenga, S. Foletti, G. Palasantzas, and K. Arikawa, "Light on the moth-eye corneal nipple array of butterflies," *Proc Biol Sci,* vol. 273, no. 1587, pp. 661-7, Mar 22 2006.

[27] M. Wang and N. Pan, "Predictions of effective physical properties of complex multiphase materials," *Materials Science and Engineering: R: Reports,* vol. 63, no. 1, pp. 1-30, 2008/12/20.

[28] A. Deinega, I. Valuev, B. Potapkin, and Y. Lozovik, "Minimizing light reflection from dielectric textured surfaces," *Journal of the Optical Society of America A,* vol. 28, no. 5, pp. 770-777, 2011/05/01.

[29] V. Janicki, J. Sancho-Parramon, and H. Zorc, "Refractive index profile modelling of dielectric inhomogeneous coatings using effective medium theories," *Thin Solid Films,* vol. 516, no. 10, pp. 3368-3373, 2008.

[30] D. A. G. Bruggeman, "Berechnung verschiedener physikalischer Konstanten von heterogenen Substanzen. I. Dielektrizitätskonstanten und Leitfähigkeiten der Mischkörper aus isotropen Substanzen," *Ann. Phys. ,* vol. 24, no. 636, 1935.

[31] W. K. Kuo, J. J. Hsu, C. K. Nien, and H. H. Yu, "Moth-Eye-Inspired Biophotonic Surfaces with Antireflective and Hydrophobic Characteristics," *ACS Appl Mater Interfaces,* vol. 8, no. 46, pp. 32021-32030, Nov 23 2016.

[32] S. Zheng, "Nanofabrication of direct positioning atomic force microscope (AFM) probes and a novel method to attain controllable lift-off," Master's, University of Waterloo, 2017.

[33] Intlvac Thin Film Corporation. *Thin film depostition systems*. Available: https://www.intlvac.com/products-services/thin-film-deposition-systems/r-d/nanochrome-i-ll

[34] Wikipedia. *Glow discharge*. Available: https://en.wikipedia.org/wiki/Glow_discharge

[35] M. Hughes. *What is DC Sputtering*. Available: http://www.semicore.com/news/94-what-is-dc-sputtering, 2016

[36] Angstrom Engineering Inc. *Magnetron sputtering overview*. Available: https://angstromengineering.com/tech/magnetron-sputtering/

[37] Lurie Nanofabrication Facility-wiki. *Low pressure chemical vapor deposition*. Available: http://lnf-wiki.eecs.umich.edu/wiki/Low_pressure_chemical_vapor_deposition

[38] Z. Cui, *Nanofabrication*, 2 ed. Springer International Publishing, 2017, p. 235.

[39] Z. Cui, *Nanofabrication*, 2 ed. Springer International Publishing, 2017, p. 239.

[40] C. D. W. Wilkinson and M. Rahman, "Dry etching and sputtering," *Philosophical Transactions of the Royal Society of London. Series A: Mathematical, Physical and Engineering Sciences,* 10.1098/rsta.2003.1307 vol. 362, no. 1814, p. 125, 2004.

[41] J. W. Coburn and H. F. Winters, "Ion- and electron-assisted gas-surface chemistry—An important effect in plasma etching," *Journal of Applied Physics,* vol. 50, no. 5, pp. 3189-3196, 1979.

[42] B. Gorowitz and R. J. Saia, "Reactive Ion Etching," in *VLSI Electronics Microstructure Science*, vol. 8, N. G. Einspruch and D. M. Brown, Eds.: Elsevier, 1984, pp. 297-339.

[43] H. Abe, M. Yoneda, and N. Fujiwara, "Developments of Plasma Etching Technology for Fabricating Semiconductor Devices," *Japanese Journal of Applied Physics,* vol. 47, no. 3, pp. 1435-1455, 2008.

[44] J. Henri, G. Han, B. Meint de, E. Miko, and F. Jan, "A survey on the reactive ion etching of silicon in microtechnology," *Journal of Micromechanics and Microengineering,* vol. 6, no. 1, p. 14, 1996.

[45] Corial Plasma Processing Solutions. *ICP-RIE technology*. Available: https://www.corial.com/en/technologies/icp-rie-inductively-coupled-plasma-reactive-ion-etching/

[46] C. Cardinaud, M.-C. Peignon, and P.-Y. Tessier, "Plasma etching: principles, mechanisms, application to micro- and nano-technologies," *Applied Surface Science,* vol. 164, no. 1, pp. 72-83, 2000/09/01.

[47] W. N. G. Hitchon, *Plasma Processes for Semiconductor Fabrication* (Cambridge Studies in Semiconductor Physics and Microelectronic Engineering). Cambridge: Cambridge University Press, 1999.

[48] Z. Diao, M. Kraus, R. Brunner, J. H. Dirks, and J. P. Spatz, "Nanostructured Stealth Surfaces for Visible and Near-Infrared Light," *Nano Lett,* vol. 16, no. 10, pp. 6610-6616, Oct 12 2016.

[49] S. A. Boden and D. M. Bagnall, "Tunable reflection minima of nanostructured antireflective surfaces," *Applied Physics Letters,* vol. 93, no. 13, p. 133108, 2008.

[50] D. A. Baranov *et al.*, "Broadband antireflective coatings based on two-dimensional arrays of subwavelength nanopores," *Applied Physics Letters,* vol. 106, no. 17, p. 171913, 2015.

[51] M. Moro, J. Taniguchi, and S. Hiwasa, "Fabrication of antireflection structure film by roll-to-roll ultraviolet nanoimprint lithography," *Journal of Vacuum Science & Technology B, Nanotechnology and Microelectronics: Materials, Processing, Measurement, and Phenomena,* vol. 32, no. 6, p. 06FG09, 2014.

[52] L. Wang *et al.*, "Maskless laser tailoring of conical pillar arrays for antireflective biomimetic surfaces," *Optics Letters,* vol. 36, no. 17, pp. 3305-3307, 2011/09/01.

[53] M. Burghoorn *et al.*, "Single Layer Broadband Anti-Reflective Coatings for Plastic Substrates Produced by Full Wafer and Roll-to-Roll Step-and-Flash Nano-Imprint Lithography," *Materials (Basel),* vol. 6, no. 9, pp. 3710-3726, Aug 27 2013.

[54] H. Sai *et al.*, "Antireflective subwavelength structures on crystalline Si fabricated using directly formed anodic porous alumina masks," *Applied Physics Letters,* vol. 88, no. 20, p. 201116, 2006.

[55] L. Li, T. Zhai, H. Zeng, X. Fang, Y. Bando, and D. Golberg, "Polystyrene sphere-assisted one-dimensional nanostructure arrays: synthesis and applications," *J. Mater. Chem.,* vol. 21, no. 1, pp. 40-56, 2011.

[56] U. C. Fischer and H. P. Zingsheim, "Submicroscopic pattern replication with visible light," *Journal of Vacuum Science and Technology,* vol. 19, no. 4, pp. 881-885, 1981.

[57] S. M. Yang, S. G. Jang, D. G. Choi, S. Kim, and H. K. Yu, "Nanomachining by colloidal lithography," *Small,* vol. 2, no. 4, pp. 458-75, Apr 2006.

[58] M. J. K. Klein, "Wafer-Scale Fabrication of Thin SiN Membranes and Au Films and Membranes with Arrays of Sub-um Holes Using Nanosphere Lithography," Doctoral dissertation, University of Lausanne, 2010.

[59] A. Chandramohan, N. V. Sibirev, V. G. Dubrovskii, M. C. Petty, A. J. Gallant, and D. A. Zeze, "Model for large-area monolayer coverage of polystyrene nanospheres by spin coating," *Sci Rep,* vol. 7, p. 40888, Jan 19 2017.

[60] P. I. Stavroulakis, N. Christou, and D. Bagnall, "Improved deposition of large scale ordered nanosphere monolayers via liquid surface self-assembly," *Materials Science and Engineering: B,* vol. 165, no. 3, pp. 186-189, 2009.

[61] W. Ferdinand *et al.*, "Stability of the hydrophilic behavior of oxygen plasma activated SU-8," *Journal of Micromechanics and Microengineering,* vol. 17, no. 3, p. 524, 2007.

[62] L. Sang-Joon, P. Bu-Geun, K. Guk-Bae, and J. Young-Gil, "Self-Cleaning Features of Plasma-Treated Surfaces with Self-Assembled Monolayer Coating," *Japanese Journal of Applied Physics,* vol. 45, no. 2R, p. 912, 2006.

[63] F. Fan and K. J. Stebe, "Assembly of Colloidal Particles by Evaporation on Surfaces with Patterned Hydrophobicity," *Langmuir,* vol. 20, no. 8, pp. 3062-3067, 2004/04/01.

[64] H. B. de Aguiar, M. L. Strader, A. G. de Beer, and S. Roke, "Surface structure of sodium dodecyl sulfate surfactant and oil at the oil-in-water droplet liquid/liquid interface: a manifestation of a nonequilibrium surface state," *J Phys Chem B,* vol. 115, no. 12, pp. 2970-8, Mar 31 2011.

[65] J. C. Hulteen, D. A. Treichel, M. T. Smith, M. L. Duval, T. R. Jensen, and R. P. Van Duyne, "Nanosphere Lithography: Size-Tunable Silver Nanoparticle and Surface Cluster Arrays," *The Journal of Physical Chemistry B,* vol. 103, no. 19, pp. 3854-3863, 1999/05/01.

[66] K. Kempa *et al.*, "Photonic Crystals Based on Periodic Arrays of Aligned Carbon Nanotubes," *Nano Letters,* vol. 3, no. 1, pp. 13-18, 2003/01/01.

[67] R. P. White and J. E. G. Lipson, "Polymer Free Volume and Its Connection to the Glass Transition," *Macromolecules,* vol. 49, no. 11, pp. 3987-4007, 2016.

[68] P. Hanarp, M. Käll, and D. S. Sutherland, "Optical Properties of Short Range Ordered Arrays of Nanometer Gold Disks Prepared by Colloidal Lithography," *The Journal of Physical Chemistry B,* vol. 107, no. 24, pp. 5768-5772, 2003/06/01.

[69] polymerdatabase.com. Polystyrenes [Online]. Available: http://polymerdatabase.com/polymer%20classes/Polystyrene%20type.html

[70] U. Gaur and B. Wunderlich, "Study of Microphase Separation in Block Copolymers of Styrene and α-Methylstyrene in the Glass Transition Region Using Quantitative Thermal Analysis," *Macromolecules,* vol. 13, no. 6, pp. 1618-1625, 1980/11/01 1980.

[71] R. Qian, L. Wu, D. Shen, D. H. Napper, R. A. Mann, and D. F. Sangster, "Single-chain polystyrene glasses," *Macromolecules,* vol. 26, no. 11, pp. 2950-2953, 1993/05/01 1993.

[72] J. Ding, G. Xue, Q. Dai, and R. Cheng, "Glass transition temperature of polystyrene microparticles," *Polymer,* vol. 34, no. 15, pp. 3325-3327, 1993/01/01/ 1993.

[73] Y. Mi, G. Xue, and X. Wang, "Glass transition of nano-sized single chain globules," *Polymer,* vol. 43, no. 25, pp. 6701-6705, 2002/01/01/ 2002.

[74] P. E. Riley, "Plasma Etching of Aluminum Metallizations for Ultralarge Scale Integrated Circuits," *Journal of The Electrochemical Society,* vol. 140, no. 5, pp. 1518-1522, May 1, 1993 1993.

[75] J. W. Lutze, A. H. Perera, and J. P. Krusius, "Anisotropic Reactive Ion Etching of Aluminum Using Cl2, BCl3, and CH 4 Gases," *Journal of The Electrochemical Society,* vol. 137, no. 1, pp. 249-252, January 1, 1990 1990.

[76] F. Saffih, C. Con, A. Alshammari, M. Yavuz, and B. Cui, "Fabrication of silicon nanostructures with large taper angle by reactive ion etching," *Journal of Vacuum Science & Technology B, Nanotechnology and Microelectronics: Materials, Processing, Measurement, and Phenomena,* vol. 32, no. 6, p. 06FI04, 2014.

[77] A. S. Franz Laermer, "Method of Anisotropically Etching Silicon," United States Patent 5501893, 1996.

[78] H. V. Jansen, M. J. de Boer, S. Unnikrishnan, M. C. Louwerse, and M. C. Elwenspoek, "Black silicon method: X. A review on high speed and selective plasma etching of silicon with profile control: an in-depth comparison between Bosch and cryostat DRIE processes as a roadmap to next generation equipment," *Journal of Micromechanics and Microengineering,* vol. 19, no. 3, 2009.

[79] D. L. Flamm and V. M. Donnelly, "The design of plasma etchants," *Plasma Chemistry and Plasma Processing,* vol. 1, no. 4, pp. 317-363, 1981/12/01.

[80] P. Harvey-Collard, A. Jaouad, D. Drouin, and M. Pioro-Ladrière, "Inductively Coupled Plasma etching of amorphous silicon nanostructures over nanotopography using C4F8/SF6 chemistry," *Microelectronic Engineering,* vol. 110, no. Supplement C, pp. 408-413, 2013/10/01.

[81] R. K. Dey, J. Shen, and B. Cui, "Oxidation sharpening of silicon tips in the atmospheric environment," *Journal of Vacuum Science & Technology B, Nanotechnology and Microelectronics: Materials, Processing, Measurement, and Phenomena,* vol. 35, no. 6, 2017.

[82] M. Mitsutoshi, I. Wataru, O. Hiroyuki, and S. Tatsuya, "Dry Thermal Oxidation of Polycrystalline and Amorphous Silicon Films for Application to Thin Film Transistors," *Japanese Journal of Applied Physics,* vol. 37, no. 3S, p. 1076, 1998.

[83] I. M. Peters, C. Ulbrich, J. C. Goldschmidt, J. Fernandez, G. Siefer, and B. Bläsi, Directionally selective light trapping in a germanium solar cell. *Opt. Express*, 19, A136-A145, 2011

[84] Y. M. Song, Y. Jeong, C. I. Yeo, and Y. T. Lee, "Enhanced power generation in concentrated photovoltaics using broadband antireflective coverglasses with moth eye structures," Optics Express, vol. 20, no. S6, pp. A916-A923, 2012/11/05.